Chapter 3

Analytical Tomographic Image Reconstruction Methods

ch,tomo

Our models of physical phenomena are merely games we play with symbols on paper [1]

Contents

s,tomo,intro

3.1 Introduction (s,tomo,intro)

The primary focus of this book is on statistical methods for tomographic image reconstruction using reasonably realistic physical models. Nevertheless, analytical image reconstruction methods, even though based on somewhat unrealistic simplified models, are important when computation time is so limited that an approximate solution is tolerable. Analytical methods are also useful for developing intuition, and for initializing iterative algorithms associated with statistical reconstruction methods. This chapter reviews classical analytical tomographic reconstruction methods. (Other names are *Fourier reconstruction methods* and *direct reconstruction methods*, because these methods are non-iterative.) Entire books have been devoted to this subject [2–6], whereas this chapter highlights only a few results. Many readers will be familiar with much of this material except perhaps for the angularly weighted backprojection that is described in §3.3. This backprojector is introduced here to facilitate analysis of *weighted least-squares* (*WLS*) formulations in Chapter 4.

There are several limitations of analytical reconstruction methods that impair their performance. Analytical methods generally ignore measurement noise in the problem formulation and treat noise-related problems as an "afterthought" by post-filtering operations. Analytical formulations usually assume continuous measurements and provide integral-form solutions. Sampling issues are treated by discretizing these solutions "after the fact." Analytical methods require certain standard geometries (*e.g.*, parallel rays and complete sampling in radial and angular coordinates). Statistical methods for image reconstruction can overcome all of these limitations.

s,tomo,radon

3.2 Radon transform in 2D (s,tomo,radon)

The foundation of analytical reconstruction methods is the *Radon transform*, which relates a 2D function $f(x,y)$ to the collection of *line integrals* of that function. (We focus on the 2D case throughout most of this chapter.) Emission and transmission tomography systems acquire measurements that are something like blurred line integrals, so the line-integral model represents an idealization of such systems. Fig. 3.2.1 illustrates the geometry of the line integrals associated with the 2D Radon transform.

3.2.1 Definition

Let $\mathcal{L}(r,\varphi)$ denote the line in the Euclidean plane at angle φ counter-clockwise from the y axis and at a signed distance r from the origin:

$$
\begin{aligned}
\mathcal{L}(r,\varphi) &= \left\{ (x,y) \in \mathbb{R}^2 : x\cos\varphi + y\sin\varphi = r \right\} & (3.2.1) \\
&= \left\{ (r\cos\varphi - \ell\sin\varphi,\ r\sin\varphi + \ell\cos\varphi) : \ell \in \mathbb{R} \right\}. & (3.2.2)
\end{aligned}
$$

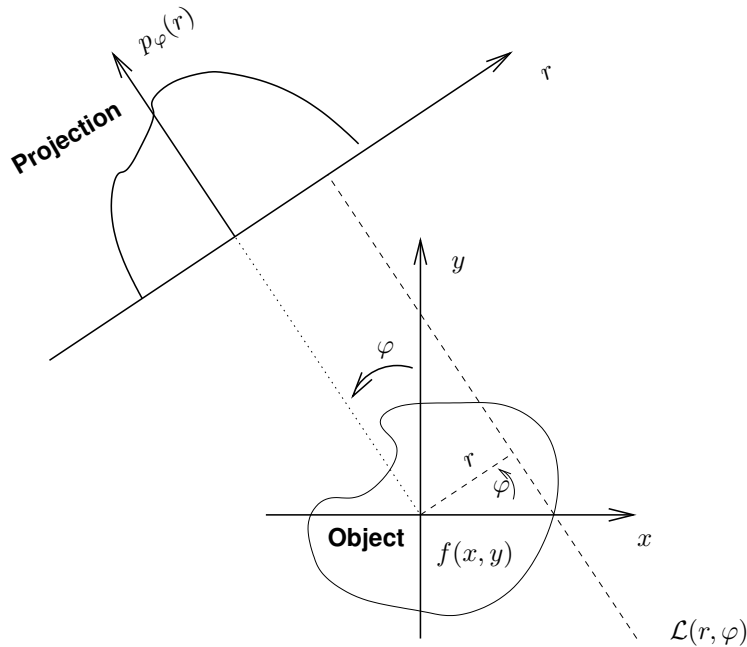e,tomo,ray

Figure 3.2.1: Geometry of the line integrals associated with the Radon transform.

Let $p_\varphi(r)$ denote the line integral through $f(x, y)$ along the line $\mathcal{L}(r, \varphi)$. There are several equivalent ways to express this line integral, each of which has its uses:

$$
\begin{aligned}
p_\varphi(r) &= \int_{\mathcal{L}(r,\varphi)} f(x, y) \, \mathrm{d}\ell \\
&= \int_{-\infty}^{\infty} f(r \cos\varphi - \ell \sin\varphi, \; r \sin\varphi + \ell \cos\varphi) \, \mathrm{d}\ell && \text{(3.2.3)} \\
&= \int_{-\infty}^{\infty} \int_{-\infty}^{\infty} f(r' \cos\varphi - \ell \sin\varphi, \; r' \sin\varphi + \ell \cos\varphi) \, \delta(r' - r) \, \mathrm{d}r' \, \mathrm{d}\ell && \text{(3.2.4)} \\
&= \int_{-\infty}^{\infty} \int_{-\infty}^{\infty} f(x, y) \, \delta(x \cos\varphi + y \sin\varphi - r) \, \mathrm{d}x \, \mathrm{d}y && \text{(3.2.5)} \\
&= \begin{cases} \dfrac{1}{|\cos\varphi|} \displaystyle\int_{-\infty}^{\infty} f\left(\dfrac{r - t \sin\varphi}{\cos\varphi}, \, t\right) \mathrm{d}t, & \cos\varphi \neq 0 \\[2ex] \dfrac{1}{|\sin\varphi|} \displaystyle\int_{-\infty}^{\infty} f\left(t, \, \dfrac{r - t \cos\varphi}{\sin\varphi}\right) \mathrm{d}t, & \sin\varphi \neq 0, \end{cases} && \text{(3.2.6)}
\end{aligned}
$$

The equation tags on the right margin: (3.2.3) labeled e,tomo,line,l; (3.2.4) labeled e,tomo,radon,r',l; (3.2.5) labeled e,tomo,line,dirac; (3.2.6) labeled e,tomo,line,xy.

where $\delta(\cdot)$ denotes the 1D *Dirac impulse*. (The last form came from [7].) The step between (3.2.4) and (3.2.5) uses the following change of variables:

$$
\begin{bmatrix} x \\ y \end{bmatrix} = \begin{bmatrix} \cos\varphi & -\sin\varphi \\ \sin\varphi & \cos\varphi \end{bmatrix} \begin{bmatrix} r' \\ \ell \end{bmatrix}. \tag{3.2.7}
$$

The *Radon transform* of f is the complete collection of line integrals[1]

$$
f \overset{\text{Radon}}{\leftrightarrow} \{p_\varphi(r) \, : \varphi \in [0, \pi], \; r \in (-\infty, \infty)\}. \tag{3.2.8}
$$

The function $p_\varphi(\cdot)$ is called the *projection* of f at angle φ. As discussed in §3.4.4, we often write $p = \mathcal{P} f$.

In its most idealized form, the *2D image reconstruction problem* is to recover $f(x, y)$ from its projections $\{p_\varphi(\cdot)\}$. To do this one must somehow return the data in projection space back to object space, as described in §3.4.

---

[1] Sometimes one refers to values of φ outside of the domain given in (3.2.8); this is possible using the "periodic extension" described in (3.2.19). Of course a practical system has a finite maximum radius that defines its circular *field of view*.
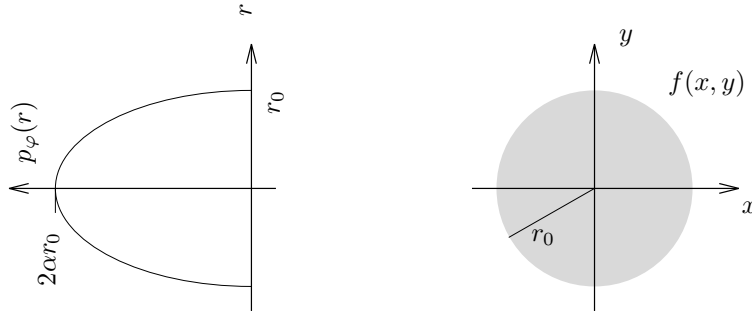
x,tomo,proj,disk **Example 3.2.1** *Consider the centered* uniform disk *object with radius* r_0:

$$f(x,y) = \alpha \operatorname{rect}\left(\frac{r}{2r_0}\right), \qquad \operatorname{rect}(t) \triangleq \mathbb{1}_{\{|t| \leq 1/2\}} = \left\{ \begin{array}{ll} 1, & |t| \leq 1/2 \\ 0, & \text{otherwise.} \end{array} \right. \qquad (3.2.9) \qquad \text{e,rect}$$

Using (3.2.3), the Radon transform of this object is:

$$\begin{aligned} p_\varphi(r) &= \int_{-\infty}^{\infty} f(r\cos\varphi - \ell\sin\varphi,\ r\sin\varphi + \ell\cos\varphi)\, \mathrm{d}\ell \\ &= \int_{-\infty}^{\infty} \alpha \operatorname{rect}\left(\frac{\sqrt{(r\cos\varphi - \ell\sin\varphi)^2 + (r\sin\varphi + \ell\cos\varphi)^2}}{2r_0}\right) \mathrm{d}\ell \\ &= \alpha \int_{-\infty}^{\infty} \operatorname{rect}\left(\frac{\sqrt{r^2 + \ell^2}}{2r_0}\right) \mathrm{d}\ell = \alpha \int_{\{\ell\ :\ r^2 + \ell^2 \leq r_0^2\}} \mathrm{d}\ell = \alpha \int_{-\sqrt{r_0^2 - r^2}}^{+\sqrt{r_0^2 - r^2}} \mathrm{d}\ell \\ &= 2\alpha \sqrt{r_0^2 - r^2} \operatorname{rect}\left(\frac{r}{2r_0}\right), \qquad\qquad\qquad\qquad\qquad\qquad \text{e,tomo,proj,disk} \\ & \qquad\qquad\qquad\qquad\qquad\qquad\qquad\qquad\qquad\qquad\qquad (3.2.10) \end{aligned}$$

which is a semi-circle function as shown in Fig. 3.2.2. These projections are independent of φ due to the circular symmetry of $f(x,y)$.

fig,tomo,disk

Figure 3.2.2: Projection of a centered uniform disk object, illustrated at $\varphi = \pi/2$.

x,tomo,proj,square **Example 3.2.2** *Consider the unit square object:*

$$f(x,y) = \operatorname{rect}(x)\operatorname{rect}(y) = \left\{ \begin{array}{ll} 1, & |x| < 1/2,\ |y| < 1/2 \\ 0, & \text{otherwise.} \end{array} \right.$$

In general the projections of this object are trapezoidal shaped functions (see Example 3.2.6 below), as illustrated in Fig. 3.2.3. At angles φ that are multiples of $\pi/2$, the trapezoid degenerates to a rectangle, and at angles that are odd multiples of $\pi/4$, the trapezoid degenerates to a triangle. Specifically, the projections are given by the following:

$$\begin{aligned} p_\varphi(r) &= l_{\max}(\varphi) \cdot \left\{ \begin{array}{ll} \dfrac{r + d_{\max}(\varphi)}{d_{\max}(\varphi) - d_{\text{break}}(\varphi)}, & -d_{\max}(\varphi) < r < -d_{\text{break}}(\varphi) \\ 1, & |r| \leq d_{\text{break}}(\varphi) \\ \dfrac{d_{\max}(\varphi) - r}{d_{\max}(\varphi) - d_{\text{break}}(\varphi)}, & d_{\text{break}}(\varphi) < r < d_{\max}(\varphi) \\ 0, & \text{otherwise,} \end{array} \right. \\[2ex] &= \left\{ \begin{array}{ll} \sqrt{2}\operatorname{tri}\left(\frac{r}{\sqrt{2}/2}\right), & \varphi = \pm\pi/4, \pm 3\pi/4, \ldots \quad \text{e,tomo,proj,square} \\ \operatorname{rect}(r), & \varphi = 0, \pm\pi/2, \pm\pi, \ldots (3.2.11) \\ \frac{1}{|\cos\varphi\sin\varphi|}\left[d_{\max}(\varphi)\operatorname{tri}\left(\frac{r}{d_{\max}(\varphi)}\right) - d_{\text{break}}(\varphi)\operatorname{tri}\left(\frac{r}{d_{\text{break}}(\varphi)}\right)\right], & \text{otherwise,} \end{array} \right. \end{aligned}$$

where e,tomo,tri

$$\operatorname{tri}(x) = (1 - |x|)\operatorname{rect}\left(\frac{x}{2}\right) \qquad\qquad\qquad\qquad (3.2.12)$$
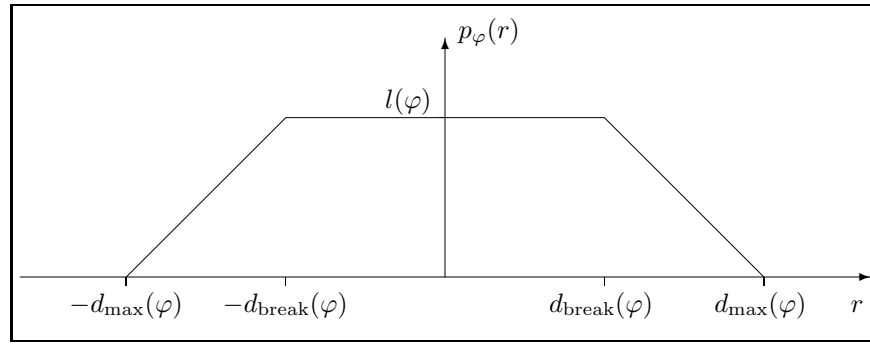
fig,tomo,square

Figure 3.2.3: The projection at angle φ of the unit square object.

denotes the unit triangle function*, and we define*

$$
\begin{aligned}
l_{\max}(\varphi) &= \frac{1}{\max(|\cos\varphi|, |\sin\varphi|)} \\
d_{\max}(\varphi) &= \frac{|\cos\varphi| + |\sin\varphi|}{2} \\
d_{\text{break}}(\varphi) &= \frac{\left||\cos\varphi| - |\sin\varphi|\right|}{2}.
\end{aligned}
$$

s,tomo,radon,polar

3.2.2   Signed polar forms (s,tomo,radon,polar)

It can be useful to have a form of the Radon transform when f is represented in a polar form. Throughout this chapter, we use a "signed polar form" $f_\circ(r, \varphi) = f(r\cos\varphi, r\sin\varphi)$, in which the radial argument r can be both positive and negative. Usually we abuse notation slightly and write $f(r, \varphi)$ without the subscript.

For making changes of variables between Cartesian coordinates and signed polar coordinates, we define

$$
r_\pm(a, b) \triangleq \begin{cases} \sqrt{a^2 + b^2}, & \{b > 0\} \text{ or } \{b = 0 \ \& \ a \geq 0\} \\ -\sqrt{a^2 + b^2}, & \{b < 0\} \text{ or } \{b = 0 \ \& \ a < 0\} \end{cases} \qquad \text{(3.2.13)}
$$

e,tomo,srad

$$
\angle_\pi(a, b) \triangleq \begin{cases} \tan^{-1}\left(\frac{b}{a}\right), & ab > 0 \\ 0, & b = 0 \\ \pi/2, & a = 0, \ b \neq 0 \\ \tan^{-1}\left(\frac{b}{a}\right) + \pi, & ab < 0. \end{cases} \qquad \text{(3.2.14)}
$$

e,tomo,angpi

These functions obey the following natural properties:

$$
\begin{aligned}
\angle_\pi(a, b) &\in [0, \pi) \\
\angle_\pi(b, a) &= \begin{cases} 0, & a = 0 \ \& \ b = 0 \\ (\pi/2 - \angle_\pi(a, b)) \bmod \pi, & \text{else} \end{cases} \\
|r_\pm(a, b)| &= \sqrt{a^2 + b^2} \\
r_\pm(\alpha a, \alpha b) &= \alpha \, r_\pm(a, b) \\
\angle_\pi(\alpha a, \alpha b) &= \angle_\pi(a, b), \qquad \alpha \neq 0 \\
\cos \angle_\pi(a, b) &= \begin{cases} 1, & b = 0 \\ a \operatorname{sgn}(b) / \sqrt{a^2 + b^2}, & b \neq 0 \end{cases} \\
\sin \angle_\pi(a, b) &= \begin{cases} 0, & b = 0 \\ |b| / \sqrt{a^2 + b^2}, & b \neq 0 \end{cases} \\
r_\pm(a, b) \cos \angle_\pi(a, b) &= a \\
r_\pm(a, b) \sin \angle_\pi(a, b) &= b.
\end{aligned}
$$

e,tomo,polar,prop
(3.2.15)

Making a change of variables $r = r_\pm(x, y)$ and $\varphi = \angle_\pi(x, y)$ leads to the following integral relationship:

$$\int_{-\infty}^{\infty} \int_{-\infty}^{\infty} f(x, y)\, \mathrm{d}x\, \mathrm{d}y = \int_0^\pi \int_{-\infty}^{\infty} f_\circ(r, \varphi)\, |r|\, \mathrm{d}r\, \mathrm{d}\varphi.$$

<div style="text-align: right">e,tomo,radon,polar,int
(3.2.16)</div>

In particular, substituting $r' = r_\pm(x, y)$ and $\varphi' = \angle_\pi(x, y)$ into the Radon transform expression (3.2.5) leads to the following Radon transform in polar coordinates:

$$p_\varphi(r) = \int_0^\pi \int_{-\infty}^{\infty} f_\circ(r', \varphi')\, \delta(r' \cos(\varphi - \varphi') - r)\, |r'|\, \mathrm{d}r'\, \mathrm{d}\varphi'$$

<div style="text-align: right">e,tomo,line,polar
(3.2.17)</div>

The properties (3.2.15) arise in several of the subsequent derivations.

3.2.3 Radon transform properties (s,tomo,radon,prop)

The following list shows a few of the many properties of the Radon transform. This list is far from exhaustive; indeed new properties continue to be found, *e.g.*, [8, 9]. Throughout this list, we assume $f(x, y) \overset{\text{Radon}}{\leftrightarrow} p_\varphi(r)$.

- **Linearity**
  If $g(x, y) \overset{\text{Radon}}{\leftrightarrow} q_\varphi(r)$, then

$$\alpha f + \beta g \overset{\text{Radon}}{\leftrightarrow} \alpha p + \beta q.$$

- **Shift / translation**

$$f(x - x_0, y - y_0) \overset{\text{Radon}}{\leftrightarrow} p_\varphi(r - x_0 \cos\varphi - y_0 \sin\varphi)$$

<div style="text-align: right">e,tomo,radon,shift
(3.2.18)</div>

- **Rotation**

$$f(x \cos\varphi' + y \sin\varphi', -x \sin\varphi' + y \cos\varphi') \overset{\text{Radon}}{\leftrightarrow} p_{\varphi - \varphi'}(r)$$

- **Circular symmetry**

$$f_\circ(r, \varphi) = f_\circ(r, 0)\ \forall\varphi \implies p_\varphi = p_0\ \forall\varphi$$

- **Symmetry/periodicity**

$$p_\varphi(r) = p_{\varphi \pm \pi}(-r) = p_{\varphi \pm k\pi}\left((-1)^k r\right), \qquad \forall k \in \mathbb{Z}$$

<div style="text-align: right">e,tomo,radon,prop,period
(3.2.19)</div>

- **Affine scaling**

$$f(\alpha x, \beta y) \overset{\text{Radon}}{\leftrightarrow} \frac{p_{\angle_\pi(\beta \cos\varphi,\, \alpha \sin\varphi)}\left(\dfrac{r|\alpha|\beta}{\sqrt{(\beta \cos\varphi)^2 + (\alpha \sin\varphi)^2}}\right)}{\sqrt{(\beta \cos\varphi)^2 + (\alpha \sin\varphi)^2}},$$

<div style="text-align: right">e,tomo,radon,prop,affine
(3.2.20)</div>

for $\alpha, \beta \neq 0$, where $r_\pm$ and $\angle_\pi$ were defined in §3.2.2.

The following two properties are special cases of the affine scaling property.
  - **Magnification/minification**

$$f(\alpha x, \alpha y) \overset{\text{Radon}}{\leftrightarrow} \frac{1}{|\alpha|} p_\varphi(\alpha r), \qquad \alpha \neq 0$$

  - **Flips**

$$f(x, -y) \overset{\text{Radon}}{\leftrightarrow} p_{\pi - \varphi}(-r)$$
$$f(-x, y) \overset{\text{Radon}}{\leftrightarrow} p_{\pi - \varphi}(r)$$

- **The *projection integral theorem***
  For a scalar function $h : \mathbb{R} \to \mathbb{R}$:

$$\begin{aligned}
\int p_\varphi(r)\, h(r)\, \mathrm{d}r &= \int \left(\int f(r \cos\varphi - \ell \sin\varphi,\, r \sin\varphi + \ell \cos\varphi)\, \mathrm{d}\ell \right) h(r)\, \mathrm{d}r \\
&= \iint f(x, y)\, h(x \cos\varphi + y \sin\varphi)\, \mathrm{d}x\, \mathrm{d}y,
\end{aligned}$$

<div style="text-align: right">e,tomo,pit
(3.2.21)</div>

by making the orthonormal coordinate rotation: $x = r \cos\varphi - \ell \sin\varphi,\ y = r \sin\varphi + \ell \cos\varphi$.
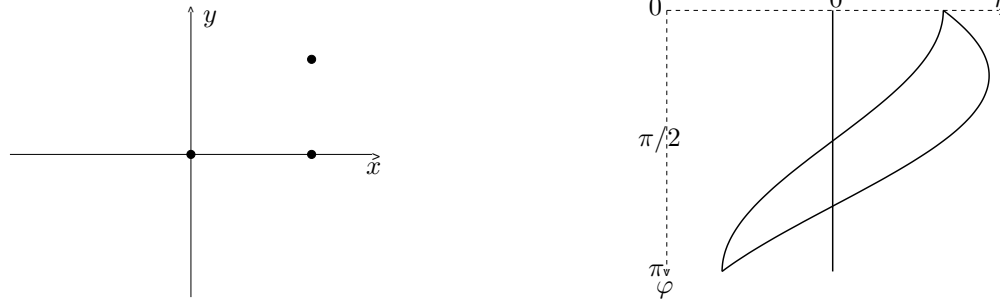
fig˙tomo˙sino˙points

Figure 3.2.4: Left: cross-section of 2D object containing three Dirac impulses. Right: the corresponding sinogram consisting of three sinusoidal impulse ridges.

- **Volume conservation**

$$\int_{-\infty}^{\infty} \int_{-\infty}^{\infty} f(x, y) \, \mathrm{d}x \, \mathrm{d}y = \int_{-\infty}^{\infty} p_\varphi(r) \, \mathrm{d}r, \qquad \forall \varphi. \tag{3.2.22}$$

e,tomo,radon,dc

This is a corollary to the projection integral theorem for $h(r) = 1$. The volume conservation property is one of many *consistency conditions* of the Radon transform [4].

The following example serves to illustrate some of these properties.

x,tomo,proj,dirac **Example 3.2.3** *Consider the object $f(x, y) = \delta_2(x - x_0, y - y_0)$, the 2D Dirac impulse centered at (x_0, y_0). This generalized function can be thought of as a disk function centered at (x_0, y_0) of radius r_0 and height $1/(\pi r_0^2)$ (so that volume is unity) in the limit as $r_0 \to 0$.*

Let $C_{r_0}(r) = 2\sqrt{r_0^2 - r^2} \operatorname{rect}\left(\frac{r}{2r_0}\right)$ denote the projection of centered uniform disk with radius r_0 as derived in (3.2.10) in Example 3.2.1. Then by the shift property (3.2.18), the projections of a disk centered at (x_0, y_0) are:

$$p_\varphi(r) = C_{r_0}(r - [x_0 \cos\varphi + y_0 \sin\varphi]).$$

(See Fig. 3.2.5 below.) Thus the projections of the 2D Dirac impulse are found as follows:

$$p_\varphi(r) = \frac{1}{\pi r_0^2} C_{r_0}(r - [x_0 \cos\varphi + y_0 \sin\varphi]) \to \delta(r - [x_0 \cos\varphi + y_0 \sin\varphi]) \quad as \ r_0 \to 0.$$

In summary, for a 2D Dirac impulse object located at (x_0, y_0), the projection at angle φ is a 1D Dirac impulse located at $r = x_0 \cos\varphi + y_0 \sin\varphi$. See Fig. 3.2.4.

3.2.4 Sinogram

Because $p_\varphi(r)$ is a function of two arguments, we can display $p_\varphi(r)$ as a 2D grayscale picture where usually r and φ are the horizontal and vertical axes respectively. If we make such a display of the projections $p_\varphi(r)$ of a Dirac impulse, then the picture looks like a sinusoid corresponding to the function $r = x_0 \cos\varphi + y_0 \sin\varphi$. Hence this 2D function is called a *sinogram* and (when sampled) represents the raw data available for image reconstruction. So the goal of tomographic reconstruction is to estimate the object $f(x, y)$ from a measured sinogram.

Each point (x, y) in object space contributes a unique sinusoid to the sinogram, with the "amplitude" of the sinusoid being $\sqrt{x^2 + y^2}$, the distance of the point from the origin, and the "phase" of the sinusoid depending on $\angle_\pi(x, y)$. A sinogram is the superposition of all of these sinusoids, each one weighted by the value $f(x, y)$. Hence it seems plausible that there could be enough information in the sinogram to recover the object f, if we can unscramble all of those sinusoids.

tomo,radon,points **Example 3.2.4** *Fig. 3.2.4 illustrates these concepts for the object $f(x, y) = \delta_2(x, y) + \delta_2(x - 1, y) + \delta_2(x - 1, y - 1)$ with corresponding projections $p_\varphi(r) = \delta(r) + \delta(r - \cos\varphi) + \delta(r - \cos\varphi - \sin\varphi)$.*

Fig. 3.2.5 shows the sinogram for a disk of radius $r_0 = 20$ centered at position $(x_0, y_0) = (40, 0)$.
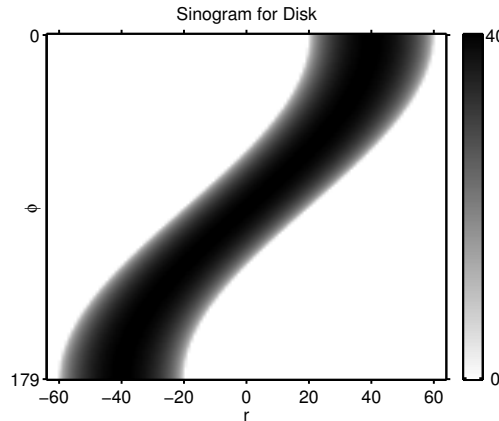
Sinogram for Disk

fig˙tomo˙disk˙sino

Figure 3.2.5: Sinogram for a disk object of radius $r_0 = 20$ centered at $(x_0, y_0) = (40, 0)$.

3.2.5 Fourier-slice theorem

The most important corollary of the projection-integral theorem (3.2.21) is the *Fourier-slice theorem*, also known as the *central-slice theorem* or *central-section theorem* or *projection-slice theorem*. In words, the statement of this theorem is as follows[2]. If $p_\varphi(r)$ denotes the Radon transform of $f(x, y)$, then the 1D Fourier transform of $p_\varphi(\cdot)$ equals the slice at angle φ through the 2D Fourier transform of $f(x, y)$.

Let $P_\varphi(\nu)$ denote the 1D Fourier transform[3] of $p_\varphi(r)$, *i.e.*,

$$P_\varphi(\nu) = \int_{-\infty}^{\infty} p_\varphi(r) \, e^{-i2\pi\nu r} \, dr.$$

Let $F(u, v)$ denote the 2D Fourier transform of $f(x, y)$, *i.e.*,

$$F(u, v) = \int_{-\infty}^{\infty} \int_{-\infty}^{\infty} f(x, y) \, e^{-i2\pi(ux + vy)} \, dx \, dy.$$ (3.2.23)

e,ft2

Then in mathematical notation, the *Fourier-slice theorem* is simply:

$$P_\varphi(\nu) = F(\nu\cos\varphi, \nu\sin\varphi) = F_\circ(\nu, \varphi), \qquad \forall \nu \in \mathbb{R}, \quad \forall \varphi \in \mathbb{R},$$ (3.2.24)

e,tomo,fst

where $F_\circ(\rho, \Phi) = F(\rho\cos\Phi, \rho\sin\Phi)$ denotes the polar form of $F(u, v)$. (Again we will frequently recycle notation and omit the subscript.) The proof of the Fourier-slice theorem is remarkably simple: merely set $h(r) = \exp(-i2\pi\nu r)$ in the projection-integral theorem (3.2.21).

It follows immediately from the Fourier-slice theorem that the Radon transform (3.2.8) describes completely any (Fourier transformable) object $f(x, y)$, because there is a one-to-one correspondence between the Radon transform and the 2D Fourier transform $F(u, v)$, and from $F(u, v)$ we can recover $f(x, y)$ by an inverse 2D Fourier transform.

x,tomo,slice,bessel **Example 3.2.5** *For the circularly symmetric Bessel object* $f(x, y) = f(r) = (\pi/2)J_0(\pi r)$, *from a table of Hankel transforms* $F(\rho) = \frac{1}{2}\delta(|\rho| - \frac{1}{2})$. *(So $F(\rho)$ is an impulse-ring of radius 1/2.) Thus* $P_\varphi(\nu) = F(\nu) = \frac{1}{2}\delta(|\nu| - \frac{1}{2}) = \frac{1}{2}\delta(\nu - \frac{1}{2}) + \frac{1}{2}\delta(\nu + \frac{1}{2})$, *so* $p_\varphi(r) = \cos(\pi r)$. *So the projections of Bessel objects are sinusoids.*

x,tomo,slice,rect **Example 3.2.6** *The 2D the uniform rectangle object and its Fourier transform are*

$$f(x, y) = \text{rect}\left(\frac{x}{a}\right)\text{rect}\left(\frac{y}{b}\right) \overset{\text{2D FT}}{\longleftrightarrow} F(u, v) = a\,\text{sinc}(au)\,b\,\text{sinc}(bv),$$

---

[2]Apparently the first publication of this result was in Bracewell's 1956 paper [10]. However, at a symposium on 2004-7-17 held at Stanford University to celebrate the 75th birthday of Albert Macovski, Ron Bracewell stated that he believes that the theorem was "well known" to other radio astronomers at the time.

[3]Being an engineer, I simply assume existence of the Fourier transforms of all functions of interest here.

so in polar form: $F_o(\rho, \Phi) = a \operatorname{sinc}(a\rho \cos\Phi) \, b \operatorname{sinc}(b\rho \sin\Phi)$. *By the Fourier slice theorem, the 1D FT of its projections are given by*

$$P_\varphi(\nu) = F_o(\nu, \varphi) = a \operatorname{sinc}(\nu a \cos\varphi) \, b \operatorname{sinc}(\nu b \sin\varphi).$$

<div align="right">e,tomo,slice,rect,Pau
(3.2.25)</div>

Thus, by the convolution property *of the FT (27.3.3), each projection is the convolution of two rect functions:*

$$p_\varphi(r) = \frac{1}{|\cos\varphi|} \operatorname{rect}\left(\frac{r}{a \cos\varphi}\right) * \frac{1}{|\sin\varphi|} \operatorname{rect}\left(\frac{r}{b \sin\varphi}\right),$$

<div align="right">e,tomo,slice,rect,proj
(3.2.26)</div>

which is a trapezoid *in general, as illustrated Fig. 3.2.3 for the case* $a = b = 1$. *(The "$*$" above denotes 1D convolution with respect to* r.)

Example 3.2.7 *The 2D FT of a uniform disk object* $f(x,y) = \operatorname{rect}\left(\frac{r}{2r_0}\right)$ *is* $F(\rho) = r_0^2 \operatorname{jinc}(r_0\rho)$.

Thus $P_\varphi(\nu) = r_0^2 \operatorname{jinc}(r_0\nu) = r_0^2 \frac{J_1(\pi r_0\nu)}{2r_0\nu}$, *where* J_1 *denotes the 1st-order* Bessel function *of the first kind. Because* $J_1(2\pi\nu)/(2\nu)$ *and* $\sqrt{1 - t^2} \operatorname{rect}(t/2)$ *are 1D Fourier transform pairs [11, p. 337], we see that the projections of a uniform disk are given by* $p_\varphi(r) = 2\sqrt{r_0^2 - r^2} \operatorname{rect}\left(\frac{r}{2r_0}\right)$. *This agrees with the result shown in (3.2.10) by integration.*

Example 3.2.8 *Consider the 2D gaussian object* $f(x,y) = f(r) = \frac{1}{w^2} \exp\left(-\pi \left(\frac{r}{w}\right)^2\right)$, *with corresponding 2D FT* $F(\rho) = \exp\left(-\pi(w\rho)^2\right)$. *By the Fourier-slice theorem:* $P_\varphi(\nu) = \exp\left(-\pi(w\nu)^2\right)$, *the inverse 1D Fourier transform of which is* $p_\varphi(r) = \frac{1}{w} \exp\left(-\pi \left(\frac{r}{w}\right)^2\right)$. *(Notice the slight change in the leading constant.) Thus the projections of a gaussian object are gaussian, which is a particularly important relationship. In fact, this property is related to the fact that two jointly gaussian random variables have gaussian marginal distributions.*

The following corollary follows directly from the Fourier-slice theorem.

Corollary 3.2.9 *(**Convolution property**.) If* $f \overset{\text{Radon}}{\leftrightarrow} p$ *and* $g \overset{\text{Radon}}{\leftrightarrow} q$ *then*

$$f(x,y) ** g(x,y) \overset{\text{Radon}}{\leftrightarrow} p_\varphi(r) * q_\varphi(r).$$

<div align="right">e,tomo,radon,conv
(3.2.27)</div>

In particular, it follows from Example 3.2.8 that 2D gaussian smoothing of an object is equivalent to 1D radial gaussian smoothing of each projection[4]:

$$f(x,y) ** \frac{1}{w^2} e^{-\pi(r/w)^2} \overset{\text{Radon}}{\leftrightarrow} p_\varphi(r) * \frac{1}{w} e^{-\pi(r/w)^2}.$$

3.3 **Backprojection** (s,tomo,back)

The Radon transform maps a 2D object $f(x,y)$ into a sinogram $p_\varphi(r)$ consisting of line integrals through the object. One approach to try to recover the object from $p_\varphi(r)$ would be to take each sinogram value and "smear" it back into object space along the corresponding ray, as illustrated in Fig. 3.3.1. This type of operation is called *backprojection* and is fundamental to tomographic image reconstruction. Unfortunately in its simplest form this procedure does not recover the object $f(x,y)$, but instead yields a blurred version of the object $f_b(x,y)$. This blurred version $f_b(x,y)$ is called a *laminogram* or *layergram* [12].

Recall from Example 3.2.3 that the projection of an impulse object centered at (x_0, y_0) is the "sinusoidal impulse" along $r = x_0 \cos\varphi + y_0 \sin\varphi$. Because each object point (x_0, y_0) contributes its own sinusoid to the sinogram, it is natural to "sum along the sinusoid" to attempt to find $f(x_0, y_0)$. (There are analogous image formation methods in other modalities such as ultrasound beamforming by delay and sum.)

When the sinogram of an asymmetric object is corrupted by noise, it is conceivable that different views will have different signal to noise ratios, so it may be useful to weight the views accordingly[5] while "summing along the sinusoid." Therefore, we analyze the following *angularly-weighted backprojection* operation:

$$f_b(x,y) = \int_0^\pi w(\varphi) \, p_\varphi(x \cos\varphi + y \sin\varphi) \, d\varphi,$$

<div align="right">e,tomo,back
(3.3.1)</div>

---

[4]Expressions of the form $f(x,y) ** h(r)$ should be interpreted as 2D convolution in Cartesian coordinates as follows: $g(x,y) = f(x,y) ** h(r) = \iint f(x-s, y-t) \, h\left(\sqrt{s^2+t^2}\right) ds \, dt$.

[5]It could also be useful to weight each ray differently, but such weighting is more difficult to analyze. Most readers should probably consider $w(\varphi) = 1$ on a first pass anyway.
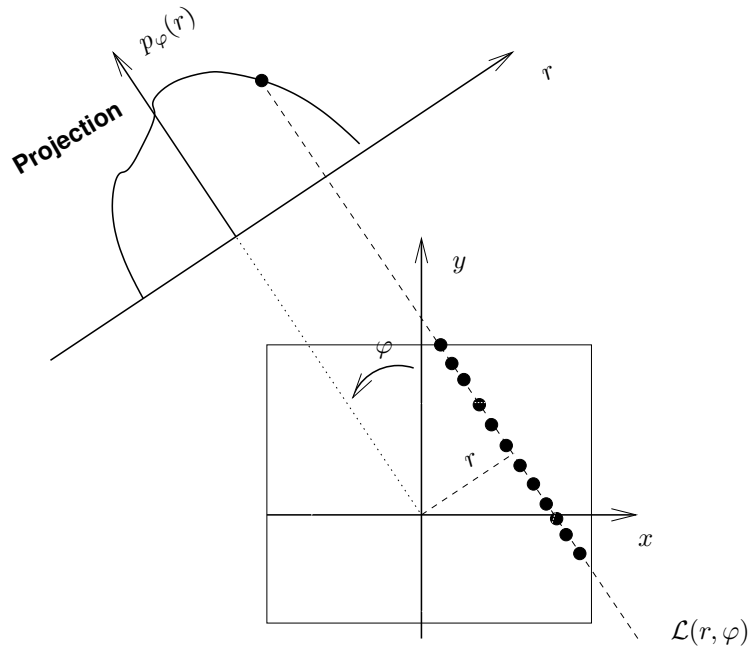
$\mathcal{L}(r, \varphi)$ fig,tomo,back

Figure 3.3.1: Illustration of back projection operation for a single projection view.

where $w(\varphi)$ denotes the user-chosen weight for angle φ. In the usual case where $w(\varphi) = 1$, this operation is the *adjoint* of the Radon transform (see §3.4.4).

3.3.1   Image-domain analysis

The following theorem shows that the laminogram $f_{\mathrm{b}}(x, y)$ is a severely blurred version of the original object $f(x, y)$.

t,tomo,1/r **Theorem 3.3.1** *If $p_\varphi(r)$ denotes the Radon transform of $f(x, y)$ as given by (3.2.3), and $f_{\mathrm{b}}(x, y)$ denotes the angularly-weighted backprojection of $p_\varphi(r)$ as given by (3.3.1), then*

$$f_{\mathrm{b}}(x, y) = h(r, \varphi) ** f(x, y), \quad where \quad h(r, \varphi) = \frac{w((\varphi + \pi/2) \bmod \pi)}{|r|}, \qquad (3.3.2)$$

e,tomo,1r

for $\varphi \in [0, \pi]$ and $r \in \mathbb{R}$.
Proof:
It is clear from (3.2.3) and (3.3.1) that the operation $f(x, y) \to p_\varphi(r) \to f_{\mathrm{b}}(x, y)$ is linear. Furthermore, this operation is shift invariant because

$$\begin{aligned}
f_{\mathrm{b}}(x - c, y - d) &= \int_0^\pi w(\varphi) \, p_\varphi((x - c) \cos\varphi + (y - d) \sin\varphi) \, \mathrm{d}\varphi \\
&= \int_0^\pi w(\varphi) \, q_\varphi(x \cos\varphi + y \sin\varphi) \, \mathrm{d}\varphi,
\end{aligned}$$

where, using the *shift property* (3.2.18), the projections $q_\varphi(r) \triangleq p_\varphi(r - c \cos\varphi - d \sin\varphi)$ denote the Radon transform of $f(x - c, y - d)$.

Due to this shift-invariance, it suffices to examine the behavior of $f_b(x, y)$ at a single location, such as the center. Using (3.2.3):

$$
\begin{aligned}
f_b(0, 0) &= \int_0^\pi w(\varphi')\, p_{\varphi'}(0)\, d\varphi' \\
&= \int_0^\pi w(\varphi') \left[\int_{-\infty}^\infty f\big(0\cos\varphi' - \ell\sin\varphi',\, 0\sin\varphi' + \ell\cos\varphi'\big)\, d\ell \right] d\varphi' \\
&= \int_0^\pi \int_{-\infty}^\infty \frac{w((\varphi + \pi/2)\bmod\pi)}{|r|}\, f(0 - r\cos\varphi,\, 0 - r\sin\varphi)\, |r|\, dr\, d\varphi, \qquad \text{(3.3.3)}
\end{aligned}
$$

making the variable changes $\varphi' = (\varphi + \pi/2)\bmod\pi$ and $\ell = \begin{cases} r, & \varphi' \in [\pi/2, \pi] \\ -r, & \varphi' \in [0, \pi/2). \end{cases}$ Thus, using the shift-invariance property noted above:

$$
f_b(x, y) = \int_0^\pi \int_{-\infty}^\infty \frac{w((\varphi + \pi/2)\bmod\pi)}{|r|}\, f(x - r\cos\varphi,\, y - r\sin\varphi)\, |r|\, dr\, d\varphi, \qquad \text{(3.3.4)}
$$

which is the convolution integral (3.3.2) in (signed) polar coordinates. □

An alternative proof uses the projection and backprojection of a centered Dirac impulse based on Example 3.2.3.

In the usual case where $w(\varphi) = 1$, we see from (3.3.2) that unmodified backprojection yields a result that is the original object blurred by the $1/r$ function. This PSF has very heavy tails, so the laminogram is nearly useless for visual interpretation. Fig. 3.3.2 illustrates the $1/r$ function.

Thus far we have focused on the parallel ray geometry implicit in (3.2.3). For a broad family of other geometries, Gullberg and Zeng [13] found appropriate pixel-dependent weighted-backprojection operations that also yield the original object convolved with $1/r$. So the nature of (3.3.2) is fairly general.
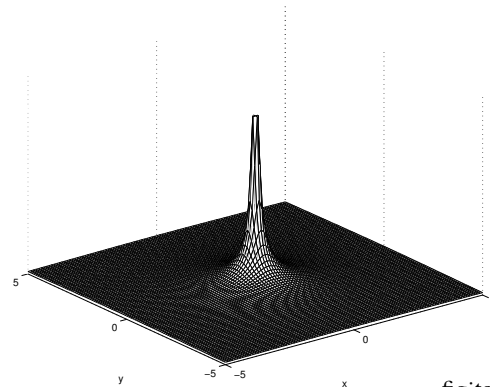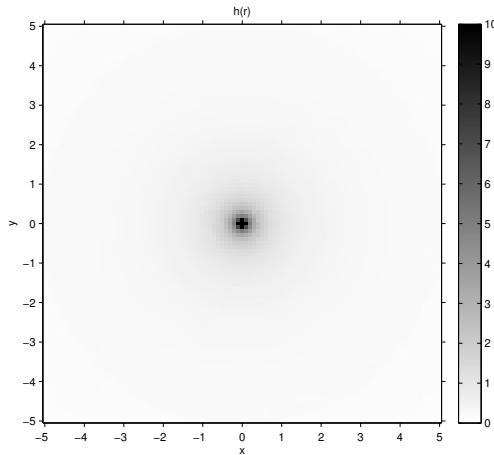
Figure 3.3.2: Illustrations of $1/r$ function and its "heavy tails."

3.3.2 Frequency-domain analysis

Because the laminogram $f_b(x, y)$ is the object $f(x, y)$ convolved with the PSF $h(r, \varphi)$ in (3.3.2), it follows that in the frequency domain we have

$$
F_b(\rho, \Phi) = H(\rho, \Phi)\, F_\circ(\rho, \Phi),
$$

where $H(\rho, \Phi)$ denotes the polar form of the 2D FT of $h(r, \varphi)$.

It is well known that $1/|r|$ and $1/|\rho|$ are 2D FT pairs [11, p. 338]. The following theorem generalizes that result to the angularly weighted case.

t,tomo,2dft,1r **Theorem 3.3.2** *The PSF given in (3.3.2) has the following 2DFT for*[6] $\Phi \in [0, \pi]$ *and* $\rho \in \mathbb{R}$:

$$h(r, \varphi) = \frac{1}{|r|} w((\varphi + \pi/2) \bmod \pi) \overset{\text{2D FT}}{\longleftrightarrow} H(\rho, \Phi) = \frac{1}{|\rho|} w(\Phi).$$

<div align="right">e,tomo,2dft,1r (3.3.5)</div>

Proof:
Evaluate the 2D FT of h:

$$
\begin{aligned}
H(\rho, \Phi) &= \int_0^\pi \int_{-\infty}^\infty h(r, \varphi) \, e^{-\imath 2\pi r\rho \cos(\varphi - \Phi)} \, |r| \, dr \, d\varphi \\
&= \int_0^\pi w((\varphi + \pi/2) \bmod \pi) \left[\int_{-\infty}^\infty e^{-\imath 2\pi r\rho \cos(\varphi - \Phi)} \, dr \right] d\varphi \\
&= \int_0^\pi w((\varphi + \pi/2) \bmod \pi) \, \delta(\rho \cos(\varphi - \Phi)) \, d\varphi \\
&= \frac{1}{|\rho|} \int_0^\pi w(\varphi') \, \delta(\sin(\varphi' - \Phi)) \, d\varphi' = \frac{1}{|\rho|} w(\Phi),
\end{aligned}
$$

letting $\varphi' = (\varphi + \pi/2) \bmod \pi$ and using[7] the following *Dirac impulse* property [11, p. 100]

$$\delta(f(t)) = \sum_{s \,:\, f(s)=0} \frac{\delta(t-s)}{\left| \dot{f}(s) \right|}.$$

<div align="right">e,tomo,back,dirac (3.3.6)</div>

In particular,

$$\delta(\sin(t)) = \sum_k \delta(t + \pi k).$$

Thus, the 2D FT of $h(r, \varphi)$ in (3.3.2) is $H(\rho, \Phi) = w(\Phi)/|\rho|$. □

So the frequency-space relationship between the laminogram and the original object is

$$F_{\mathrm{b}}(\rho, \Phi) = \frac{w(\Phi)}{|\rho|} F_\circ(\rho, \Phi).$$

<div align="right">e,tomo,lamino,1rho (3.3.7)</div>

High spatial frequencies are severely attenuated by the $1/|\rho|$ term, so the laminogram is very blurry. However, the relationship (3.3.7) immediately suggests a "deconvolution" method for recovering $f(x, y)$ from $f_{\mathrm{b}}(x, y)$, as described in the next section.

More generally, if $q_\varphi(r)$ is an arbitrary sinogram to which we apply a weighted backprojection of the form (3.3.1), then the Fourier transform of the resulting image is

$$F_{\mathrm{b}}(\rho, \Phi) = \frac{w(\Phi)}{|\rho|} Q_\varphi(\nu) \Big|_{\nu=\rho,\ \varphi=\Phi} = \frac{w(\Phi)}{|\rho|} \begin{cases} Q_\Phi(\rho), & \Phi \in [0, \pi) \\ Q_{\Phi-\pi}(-\rho), & \Phi \in [\pi, 2\pi), \end{cases}$$

<div align="right">e,tomo,back,general (3.3.8)</div>

where $Q_\varphi(\nu)$ is the 1D FT of $q_\varphi(r)$ along r. (See Problem 3.15.) The special case (3.3.7) follows from the Fourier-slice theorem.

Summary

Fig. 3.3.3 summarizes the various Fourier-transform relationships described above, as well as the Fourier-slice theorem, and the projection and backprojection operations.

x,tomo,back **Example 3.3.3** *Fig. 3.3.4 shows an object* $f(x, y)$ *consisting of two squares, the larger of which has several small holes in it. Also shown is the sinogram* $p_\varphi(r)$ *of this object. The laminogram* $f_{\mathrm{b}}(x, y)$ *is so severely blurred that the small holes are not visible.*

---

[6] Alternatively we could write $H(\rho, \Phi) = \frac{1}{|\rho|} w(\Phi \bmod \pi)$ for $\Phi \in [0, 2\pi)$ and $\rho \geq 0$.

[7] Some readers may question the rigor of this proof, and well they should because the function $1/|r|$ is not square integrable so the existence of its 2D FT is questionable. Apparently this transform pair belongs in the family that includes Dirac impulses, sinusoids, step functions, etc.

Figure 3.3.3: Relationships between a 2D object $f(x, y)$ and its projections and transforms. Left side of the figure is image domain, right side is projection domain. Inner ring is space domain, outer ring is frequency domain.

3.4 Radon transform inversion (s,tomo,iradon)

By manipulating the expressions derived in the preceding sections, one can find several methods for inverting the Radon transform, *i.e.*, for recovering an object $f(x, y)$ from its projections $\{p_\varphi(r)\}$. This section describes three alternatives: *direct Fourier reconstruction* based on the Fourier-slice theorem, the *backproject-filter* (BPF) method based on the laminogram, and finally the *convolve-backproject* (CBP) method, also called the filter-backproject (FBP) method. Each of these methods uses some of the relationships shown in Fig. 3.3.3.

In this section we continue to treat the idealized version of the tomography problem in which the entire continuum of projections $\{p_\varphi(r)\}$ is available. In practical tomography systems, only a discrete set of projections and rays are available; these sampling considerations will be addressed in §4.3 and §3.5.

3.4.1 Direct Fourier reconstruction

The *direct Fourier reconstruction* method is based directly on the Fourier-slice theorem (3.2.24). To reconstruct $f(x, y)$ from $\{p_\varphi(r)\}$ by the direct Fourier method, one performs the following steps.
- Take the 1D FT of each $p_\varphi(\cdot)$ to get $P_\varphi(\cdot)$ for each φ.
- Create a polar representation $F_\circ(\rho, \Phi)$ of the 2D FT of object $F(u, v)$ using the Fourier-slice relationship:

$$F_\circ(\rho, \varphi) = P_\varphi(\rho).$$

- Convert from polar representation $F_\circ(\rho, \Phi)$ to Cartesian coordinates $F(u, v)$. This approach, first proposed in [14], was "the first applicable method for reconstructing pictures from their projections" [15].
  For sampled data, this polar to Cartesian step, often called *gridding*, requires very careful interpolation. Fig. 3.4.1 illustrates the process. Numerous papers have considered this step in detail, *e.g.*, [7, 10, 16–39]. Of these, the
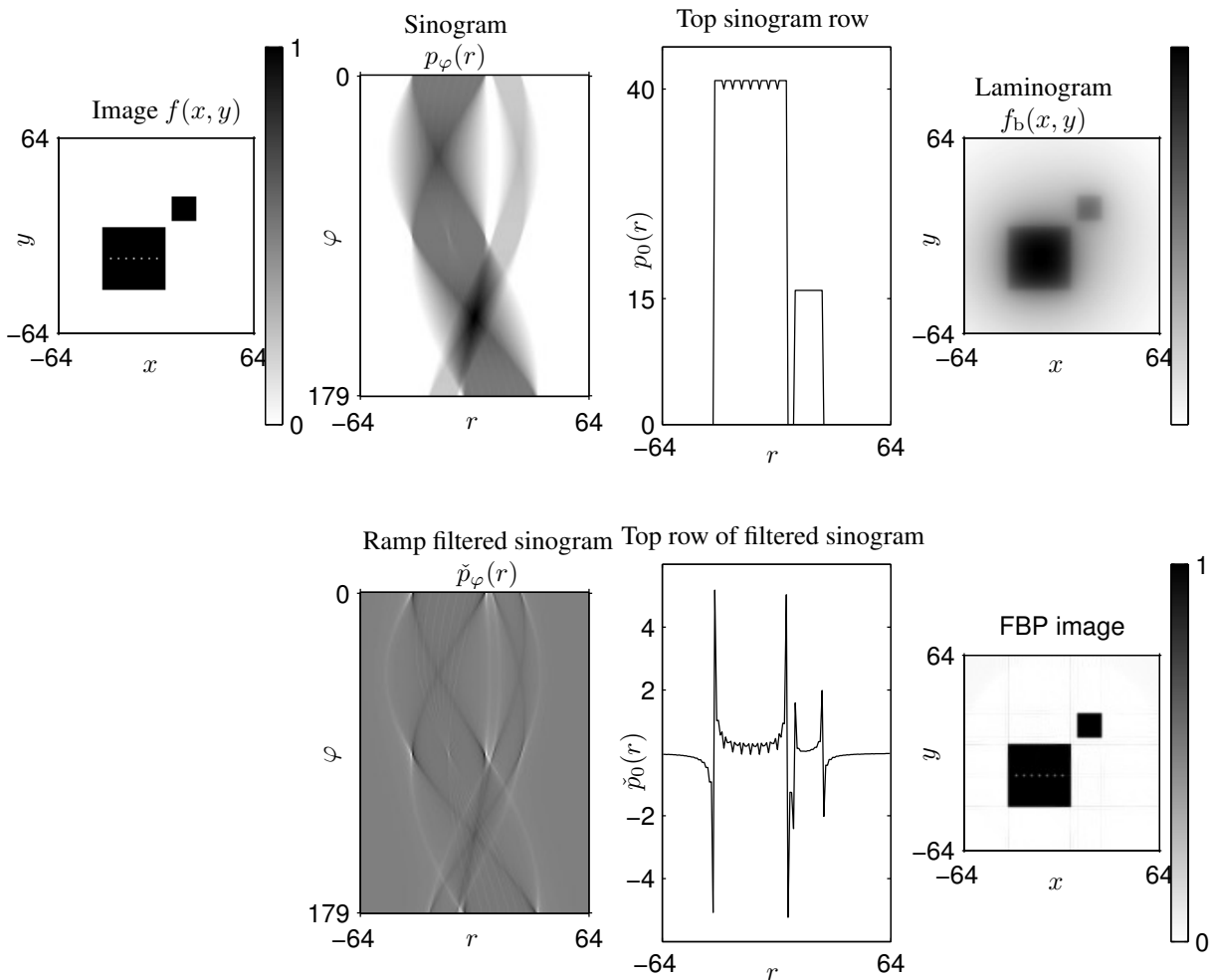
Figure 3.3.4: Illustration of FBP method. Top row: a square object $f(x,y)$, its sinogram $p_\varphi(r)$, and its laminogram $f_{\mathrm{b}}(x,y)$. Bottom row: the ramp-filtered sinogram $\check{p}_\varphi(r)$, and filter-backproject image $\hat{f}(x,y)$. Because of the ramp filtering described in §3.4.3, the small details are recovered.

fig tomo lamino

NUFFT methods with good interpolation kernels are particularly appealing, *e.g.*, [29, 38, 40]. See Chapter 6 for related problems.

• Take the inverse 2D FT of $F(u,v)$ to get $f(x,y)$.

In practice this is implemented using the 2D inverse FFT, which requires Cartesian samples, whereas the relationship $F_\circ(\rho,\varphi) = P_\varphi(\rho)$ is intrinsically polar. Hence the need for interpolation.

This method would work perfectly if given noiseless, continuous projections $p_\varphi(r)$. Practical disadvantages of this method are that it requires 2D FTs, and gridding can cause interpolation artifacts. An alternative approach uses a *Hankel transform* rather than Fourier transforms [41]; this also uses interpolation.

x,tomo,direct **Example 3.4.1** *Consider the sinogram described by*

$$p_\varphi(r) = \mathrm{rect}\left(\frac{r - x_0 \cos\varphi - y_0 \sin\varphi}{w} \right).$$

What is the object $f(x,y)$ that has these projections?

First, taking the 1D FT yields

$$P_\varphi(\nu) = w \operatorname{sinc}(w\nu)\, \mathrm{e}^{-\imath 2\pi \nu (x_0 \cos\varphi + y_0 \sin\varphi)},$$
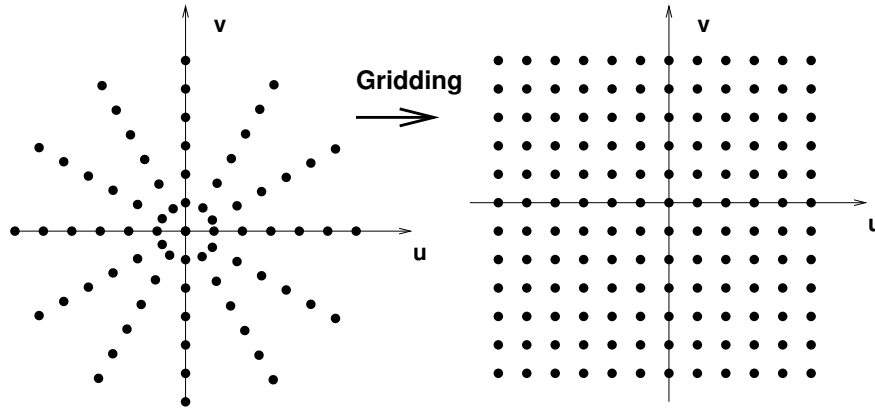
Figure 3.4.1: Illustration of polar samples of $F_\circ(\rho, \varphi) = P_\varphi(\rho)$ that must be interpolated onto Cartesian samples of $F(u, v)$.

so by the Fourier-slice theorem the spectrum of $f(x, y)$ is given by

$$F_\circ(\rho, \Phi) = w \operatorname{sinc}(w\rho) \, \mathrm{e}^{-\imath 2\pi\rho(x_0 \cos\Phi + y_0 \sin\Phi)}$$

or equivalently

$$F(u, v) = w \operatorname{sinc}\left(w\sqrt{u^2 + v^2}\right) \mathrm{e}^{-\imath 2\pi(x_0 u + y_0 v)}.$$

Because [11, p. 338], $w \operatorname{sinc}(w\rho) \overset{\text{2D FT}}{\longleftrightarrow} \frac{1}{\pi} \frac{\operatorname{rect}(r/w)}{\sqrt{(w/2)^2 - r^2}}$, the corresponding object is

$$f(x, y) = \operatorname{rect}\left(\frac{\sqrt{(x - x_0)^2 + (y - y_0)^2}}{w}\right) \frac{1}{\pi\sqrt{(w/2)^2 - (x - x_0)^2 - (y - y_0)^2}}.$$

In other words, the object that has "flat" projections has a circular singularity. De Man et al. *used this relationship to analyze the deficiencies of simplistic pixel-driven forward projection [42].*

3.4.2 The backproject-filter (BPF) method (s,tomo,bpf)

Another reconstruction method is suggested by the Fourier relationship (3.3.7) between the laminogram and the original object. Solving (3.3.7) for the 2D FT of the object yields

$$\hat{F}(u, v) = \frac{\sqrt{u^2 + v^2}}{w(\angle_\pi(u, v))} F_\mathrm{b}(u, v), \qquad\qquad (3.4.1)$$

where $F_\mathrm{b}(u, v)$ denotes the 2D FT of the laminogram, and $\angle_\pi$ was defined in (3.2.14). The filter with frequency response $|\rho| = \sqrt{u^2 + v^2}$ is called the *cone filter* due to its shape. (This method is also called the *ρ-filtered layergram* approach [12] [4, p. 153].)

The above relationship suggests the following reconstruction method.
- Choose a *nonzero* angular weighting function $w(\varphi)$.
- Perform angularly-weighted backprojection of the sinogram $p_\varphi(r)$ to form the laminogram $f_\mathrm{b}(x, y)$ using (3.3.1).
- Take the 2D FT of $f_\mathrm{b}(x, y)$ to get $F_\mathrm{b}(u, v)$.
- Apply the angularly-modulated cone filter in the Fourier domain using (3.4.1).
- The cone filter nulls the *DC component* of $f(x, y)$. This component can be recovered using the *volume conservation property* (3.2.22) of the Radon transform. For noisy sinogram data, one can compute such an integral for all projections and take the average value to estimate the DC component: $\hat{F}(0, 0) = \frac{1}{\pi} \int_0^\pi \left[\int p_\varphi(r) \, \mathrm{d}r\right] \mathrm{d}\varphi$.
- Take the inverse 2D FT of $\hat{F}(u, v)$ to get $\hat{f}(x, y)$.

This approach is called the *backproject-filter* (*BPF*) method because we first backproject the sinograms, and then apply the cone filter to "deconvolve" the $1/|\rho|$ effect of the backprojection.

In practice, using the cone-filter without modification would excessively amplify high-frequency noise. To control noise, the cone-filter is usually apodized in the frequency domain with a windowing function. Specifically, we replace (3.4.1) by

$$\hat{F}(u,v) = A(u,v) \frac{\sqrt{u^2 + v^2}}{w(\angle_\pi(u,v))} F_{\mathrm{b}}(u,v),$$

where $A(u,v)$ is an apodizing lowpass filter. In the absence of noise, the resulting reconstructed image satisfies

$$\hat{f}(x,y) = a(x,y) ** f(x,y),$$

where $a(x,y)$ is the inverse 2D FT of $A(u,v)$. (See [43, 44] for early 3D versions of BPF.)

One practical difficulty with the BPF reconstruction method is that the laminogram $f_{\mathrm{b}}(x,y)$ has unbounded spatial support (even for a finite-support object f) due to the tails of the $1/|r|$ response in (3.3.2). In practice the support of $f_{\mathrm{b}}(x,y)$ must be truncated to a finite size for computer storage, and such truncation of tails can cause problems with the deconvolution step. Furthermore, using 2D FFTs to apply the cone filter results in *periodic convolution* which can cause wrap-around effects due to the high-pass nature of the cone filter. To minimize artifacts due to spatial truncation and periodic convolution, one must evaluate $f_{\mathrm{b}}(x,y)$ numerically onto a support grid that is considerably larger than the support of the object $f(x,y)$. A large support increases the computational costs of both the backprojection step and the 2D FFT operations used for the cone filter. The FBP reconstruction method, described next, largely overcomes this limitation. The FBP method has the added benefit of only requiring 1D Fourier transforms, whereas the direct Fourier and BPF methods require 2D transforms.

tomo,bpf,cone,exp **Example 3.4.2** *For theoretical analysis, a convenient choice for the apodizer is $A(\rho) = \mathrm{e}^{-a\rho}$. Using Hankel transforms [11, p. 338] and the Laplacian property (27.3.5):*

$$-4\pi^2 r^2 h(r) \overset{\text{Hankel}}{\longleftrightarrow} \frac{1}{\rho}\frac{\mathrm{d}}{\mathrm{d}\rho}H(\rho) + \frac{\mathrm{d}^2}{\mathrm{d}\rho^2}H(\rho),$$

one can show that that the corresponding impulse response of the apodized cone filter is given by

$$h(r) = 4\pi \frac{a^2 - 2\pi^2 r^2}{(a^2 + 4\pi^2 r^2)^{5/2}} \overset{\text{Hankel}}{\longleftrightarrow} \rho\,\mathrm{e}^{-a\rho}.$$

Taking the limit as $a \to 0$ shows that $h(r) = -1/(4\pi^2 r^3)$ for $r \neq 0$, and that $h(r)$ has a singularity at $r = 0$.
Fig. 3.4.2 illustrates this impulse response for the case $a = 1$.

tomo,bpf,cone,rect **Example 3.4.3** *If we band-limit the cone filter by choosing $A(\rho) = \mathrm{rect}\left(\frac{\rho}{2\rho_{\max}}\right)$, then the resulting impulse response $h(r)$ has a complicated expression that depends on both Bessel functions and the* Struve function *[45]. Fig. 3.4.3 illustrates this impulse response for the case $\rho_{\max} = 1$.*

s,tomo,fbp

3.4.3 The filter-backproject (FBP) method (s,tomo,fbp)

We have seen that an unfiltered backprojection yields a blurry laminogram that must be deconvolved by a cone filter to yield the original image. The steps involved look like the following:

$$f(x,y) \rightarrow \boxed{\text{Projection}} \rightarrow p_\varphi(r) \rightarrow \boxed{\text{Backprojection}} \rightarrow f_{\mathrm{b}}(x,y) \rightarrow \boxed{\text{Cone filter}} \rightarrow f(x,y)\,.$$

$$\underbrace{\hphantom{f(x,y) \rightarrow \boxed{\text{Projection}} \rightarrow p_\varphi(r) \rightarrow \boxed{\text{Backprojection}}}}_{\text{convolution with } 1/|r|}$$

Because the cascade of the first two operations is linear and shift invariant, as shown in §3.3, in principle we could move the cone filter to be the first step to obtain the same overall result:

$$f(x,y) \rightarrow \boxed{\text{Cone filter}} \rightarrow \check{f}(x,y) \rightarrow \boxed{\text{Projection}} \rightarrow \check{p}_\varphi(r) \rightarrow \boxed{\text{Backprojection}} \rightarrow f(x,y),$$
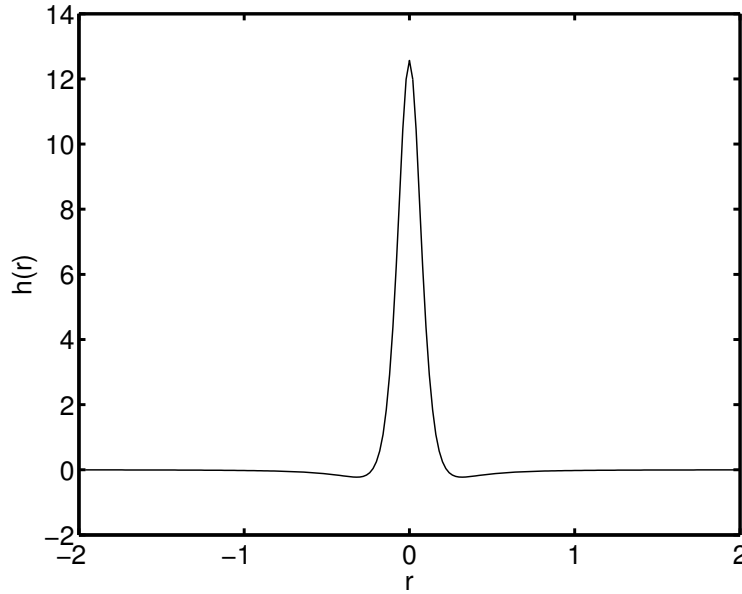
fig˙tomo˙bpf˙cone˙exp

Figure 3.4.2: Impulse response of cone filter that is apodized by a an exponential.

where, assuming $w(\varphi) = 1$ hereafter, the filtered object $\check{f}(x, y)$ has the following the spectrum:

$$\check{F}(\rho, \Phi) = |\rho| \, F_\circ(\rho, \Phi) \,.$$

Of course in practice we cannot filter the object before acquiring its projections. However, applying the Fourier-slice theorem to the scenario above, we see that each projection $\check{p}_\varphi(r)$ has the following 1D FT:

$$\check{p}_\varphi(r) \xleftrightarrow{\text{FT}} \check{P}_\varphi(\nu) = \check{F}(\rho, \varphi)\Big|_{\rho = \nu} = |\rho| \, F_\circ(\rho, \varphi)\Big|_{\rho = \nu} = |\nu| \, F_\circ(\nu, \varphi) = |\nu| \, P_\varphi(\nu) \,.$$

This relationship implies that we can replace the cone filter above with a set of 1D filters with frequency response $|\nu|$ applied to each projection $p_\varphi(\cdot)$. This filter is called the *ramp filter* due to its shape. The block diagram above becomes:

$$f(x, y) \rightarrow \boxed{\text{Projection}} \rightarrow p_\varphi(r) \rightarrow \boxed{\text{Ramp filters}} \rightarrow \check{p}_\varphi(r) \rightarrow \boxed{\text{Backprojection}} \rightarrow f(x, y) \,.$$

This reconstruction approach is called the filter-backproject (FBP) method, and is used the most widely in tomography.

A formal derivation of the FBP method uses the Fourier-slice theorem as follows:

$$
\begin{aligned}
f(x, y) &= \iint F(u, v) \, e^{-\imath 2\pi (xu + yv)} \, du \, dv \\
&= \int_0^\pi \int_{-\infty}^\infty F(\nu \cos\varphi, \nu \sin\varphi) \, e^{-\imath 2\pi \nu (x \cos\varphi + y \sin\varphi)} \, |\nu| \, d\nu \, d\varphi \\
&= \int_0^\pi \int_{-\infty}^\infty P_\varphi(\nu) \, e^{-\imath 2\pi \nu (x \cos\varphi + y \sin\varphi)} \, |\nu| \, d\nu \, d\varphi \\
&= \int_0^\pi \check{p}_\varphi(x \cos\varphi + y \sin\varphi) \, d\varphi,
\end{aligned}
$$

where we define the filtered projection $\check{p}_\varphi(r)$ as follows:

e,tomo,fbp,ramp

$$\check{p}_\varphi(r) = \int_{-\infty}^\infty P_\varphi(\nu) \, |\nu| \, e^{\imath 2\pi \nu r} \, d\nu \,. \tag{3.4.2}$$

The steps of the FBP method are summarized as follows.
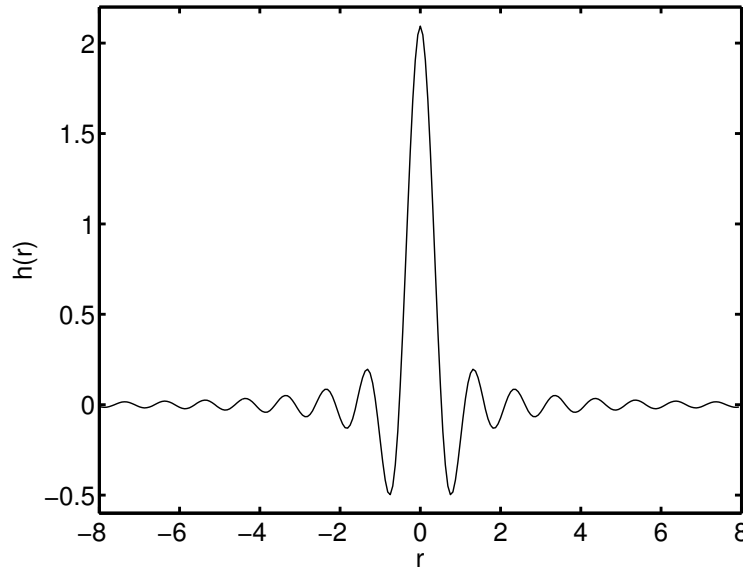
fig˙tomo˙bpf˙cone˙rect

Figure 3.4.3: Impulse response of band-limited cone filter.

- For each projection angle φ, compute the 1D FT of the projection $p_\varphi(\cdot)$ to form $P_\varphi(\nu)$.
- Multiply $P_\varphi(\nu)$ by $|\nu|$ (ramp filtering).
- For each φ, compute the inverse 1D FT of $|\nu| P_\varphi(\nu)$ to get the filtered projection $\check{p}_\varphi(r)$ in (3.4.2). In practice this filtering is often done using an FFT, which yields *periodic convolution*. Because the space-domain kernel corresponding to $|\nu|$ is not space limited (see Fig. 3.4.5), periodic convolution can cause "wrap-around" artifacts. With care, these artifacts can be avoided by zero padding the sinogram. Sampling the ramp filter can also cause aliasing artifacts. See Example 3.4.6 below for a preferable approach.
- The ramp filter nulls the DC component of each projection. If desired, this can be restored using the *volume conservation property* (3.2.22). The approach of Example 3.4.6 avoids the need for any such DC correction. Discretizing the integrals carefully avoids the need for empirical scale factors.
- Backproject the filtered sinogram $\{\check{p}_\varphi(r)\}$ using (3.3.1) to get $\hat{f}(x,y)$, *i.e.*

$$\hat{f}(x,y) = \int_0^\pi \check{p}_\varphi(x\cos\varphi + y\sin\varphi)\,\mathrm{d}\varphi\,. \tag{3.4.3}$$

e,tomo,fbp

In practice usually the *pixel-driven backprojection* approach of §3.5.3 is used.

With some hindsight, the existence of such an approach seems natural because the Fourier-slice theorem provides a relationship between the 2D FT in object domain and the 1D FT in projection domain.

s,tomo,hilbert

3.4.4 Ramp filters and Hilbert transforms

It can be useful to relate the ramp filter $|\nu|$ to a combination of differentiation and a Hilbert transform.

The *Hilbert transform* of a 1D function $f(t)$ is defined (using *Cauchy principal values*) by[8] [47, p. 248]:

$$f_{\text{Hilbert}}(t) = \frac{1}{\pi} \int_{-\infty}^{\infty} \frac{1}{t-s} f(s)\,\mathrm{d}s = \frac{1}{\pi t} * f(t). \tag{3.4.4}$$

e,tomo,hilbert

Note that this "transform" returns another function of t. The corresponding relationship in the frequency domain is

$$F_{\text{Hilbert}}(\nu) = -\imath\,\text{sgn}(\nu)\,F(\nu). \tag{3.4.5}$$

e,tomo,hilbert,freq

x,tomo,hilbert,rect **Example 3.4.4** *The Hilbert transform of the* rect *function* $\text{rect}(t) = \mathbb{1}_{\{|t|\leq 1/2\}}$ *is [47, p. 249]:* $\frac{1}{\pi}\log\left|\frac{t+1/2}{t-1/2}\right|$.

---

[8] Note that some texts use the opposite sign, *e.g.*, [11, p. 359] [46, p. 194].

Using the Hilbert transform frequency response (3.4.5), we rewrite the ramp filter $|\nu|$ in (3.4.2) as follows:

$$|\nu| = \frac{1}{2\pi} \left(\imath 2\pi\nu\right)\left(-\imath\,\mathrm{sgn}(\nu)\right).$$

The term $(\imath 2\pi\nu)$ corresponds to differentiation, by the differentiation property of the Fourier transform. Therefore, another expression for the FBP method (3.4.3) is

$$\hat{f}(x,y) = \frac{1}{2\pi}\int_0^\pi \frac{\mathrm{d}}{\mathrm{d}r}p_{\mathrm{Hilbert}}(r,\varphi)\bigg|_{r=x\cos\varphi+y\sin\varphi}\,\mathrm{d}\varphi, \qquad\qquad \begin{array}{r}\text{e,tomo,fbp,hilbert}\\(3.4.6)\end{array}$$

where $p_{\mathrm{Hilbert}}(r,\varphi)$ denotes the Hilbert transform of $p_\varphi(r)$ with respect to r. Combining (3.4.4) and (3.4.6) yields

$$\hat{f}(x,y) = \frac{1}{2\pi^2}\int_0^\pi \int_{-\infty}^\infty \frac{\frac{\partial}{\partial r}p_\varphi(r)}{x\cos\varphi+y\sin\varphi-r}\,\mathrm{d}r\,\mathrm{d}\varphi\,. \qquad\qquad \begin{array}{r}\text{e,tomo,cbp,radon}\\(3.4.7)\end{array}$$

This form is closer to Radon's inversion formula [4, p. 21] [48, 49].

x,tomo,fbp,rect **Example 3.4.5** *Continuing Example 3.2.6, the spectrum of the projection at angle φ of a rectangle object is given by (3.2.25), so its ramp-filtered projections are given by (for $\sin\varphi \neq 0$):*

$$\begin{aligned}\check{P}_\varphi(\nu) &= |\nu|\,a\,\mathrm{sinc}(\nu a\cos\varphi)\,b\,\mathrm{sinc}(\nu b\sin\varphi)\\[4pt] &= \frac{1}{\pi\cos\varphi\sin\varphi}\sin(\pi\nu a\cos\varphi)\,\mathrm{sgn}(\nu)(b\sin\varphi)\,\mathrm{sinc}(\nu b\sin\varphi)\\[4pt] &= \frac{1}{2\pi\cos\varphi\sin\varphi}\left(\mathrm{e}^{-\imath\pi\nu a\cos\varphi}-\mathrm{e}^{\imath\pi\nu a\cos\varphi}\right)\left[\imath\,\mathrm{sgn}(\nu)(b\sin\varphi)\,\mathrm{sinc}(\nu b\sin\varphi)\right].\end{aligned}$$

Using the Hilbert transform *in Example 3.4.4, the inverse 1D FT of the bracketed term is* $\frac{1}{\pi b\sin\varphi}\log\left|\frac{x-\frac{1}{2}b\sin\varphi}{x+\frac{1}{2}b\sin\varphi}\right|$, *so by the* shift property of the FT*, the filtered projections are:*

$$\check{p}_\varphi(r) = \frac{1}{2\pi^2\cos\varphi\,\sin\varphi}\log\left|\frac{r^2-\left(\frac{a\cos\varphi+b\sin\varphi}{2}\right)^2}{r^2-\left(\frac{a\cos\varphi-b\sin\varphi}{2}\right)^2}\right|,$$

cf. [50, eqn. (14)]. Fig. 3.4.4 shows an example of the projection $p_\varphi(r)$ of a unit square and its filtered version $\check{p}_\varphi(r)$. The ramp filter causes singularities at each of the points of discontinuity in the projections. (Compare with Fig. 3.3.4.) For the case $\sin\varphi = 0$, see Problem 3.23.

3.4.5 Filtered versus unfiltered backprojection

Recall that an unfiltered backprojection of a sinogram gives an image blurred by $1/|r|$. This blurring is due to the fact that the (all nonnegative) projection values "pile up" in the laminogram, and there is no destructive interference. In contrast, after filtering with the ramp filter, the projections have both positive and negative values, so destructive interference can occur, which is desirable for the parts of the image that are supposed to be zero for example. Fig. 3.3.4 illustrates these concepts.

s,tomo,cbp
3.4.6 The convolve-backproject (CBP) method

The ramp filter amplifies high frequency noise, so in practice one must apodize it by a 1D lowpass filter $A(\nu)$, in which case (3.4.2) is replaced by

$$\check{p}_\varphi(r) = \int_{-\infty}^\infty P_\varphi(\nu)\,A(\nu)\,|\nu|\,\mathrm{e}^{\imath 2\pi\nu r}\,\mathrm{d}\nu\,. \qquad\qquad \begin{array}{r}\text{e,tomo,fbp,A(u)}\\(3.4.8)\end{array}$$

Alternatively, one can perform this filtering operation in the spatial domain by radial convolution:

$$\check{p}_\varphi(r) = p_\varphi(r) * h_{\mathrm{a}}(r) = \int p_\varphi(r')\,h_{\mathrm{a}}(r-r')\,\mathrm{d}r', \qquad\qquad \begin{array}{r}\text{e,tomo,cbp,conv}\\(3.4.9)\end{array}$$
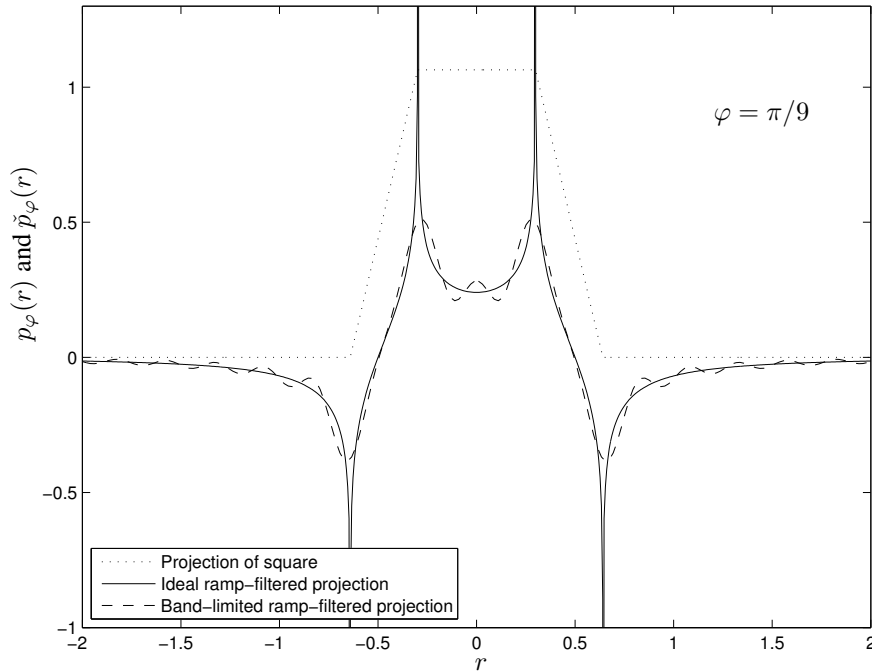
Figure 3.4.4: Projection $p_\varphi(r)$ of a unit square at angle $\varphi = \pi/9$ and its filtered versions $\check{p}_\varphi(r)$ both for ideal ramp filter $|\nu|$ and a band-limited ramp filter with cutoff frequency $\nu_0 = 4$.

where the filter kernel $h_{\mathrm{a}}(r)$ is the inverse FT of $H_{\mathrm{a}}(\nu) = A(\nu)\,|\nu|$, *i.e.*,

$$h_{\mathrm{a}}(r) = \int_{-\infty}^{\infty} A(\nu)\,|\nu|\,\mathrm{e}^{\imath 2\pi\nu r}\,\mathrm{d}\nu\,. \qquad\text{(3.4.10)}$$

<div style="text-align:right">e,tomo,cbp,h</div>

Combining with (3.4.3) and (3.4.9) leads to the following *convolve-backproject* method:

$$\hat{f}(x,y) = \int_0^\pi (p_\varphi * h_{\mathrm{a}})(x\cos\varphi + y\sin\varphi)\,\mathrm{d}\varphi = \int_0^\pi \int p_\varphi(r)\,h_{\mathrm{a}}(x\cos\varphi + y\sin\varphi - r)\,\mathrm{d}r\,\mathrm{d}\varphi\,. \qquad\text{(3.4.11)}$$

<div style="text-align:right">e,tomo,cbp</div>

Although the convolution kernel $h_{\mathrm{a}}(r)$ usually is not space-limited, the object (and hence its projections) are space limited, so space-domain convolution is feasible. On the other hand, the space-domain convolution requires more computation than a frequency-space implementation using the FFT method, so the FBP approach is often more attractive than the CBP approach.

Example 3.4.6 *As a concrete example, consider the case of a rectangular band-limiting window*

$$A(\nu) = \mathrm{rect}\left(\frac{\nu}{2\nu_0}\right), \qquad\text{(3.4.12)}$$

<div style="text-align:right">e,tomo,fbp,apod,rect</div>

which is a logical choice when the object (and hence its projections) are band limited to a maximum spatial frequency u_0. In this case, the band-limited ramp filter *has the frequency response shown in Fig. 3.4.5. This is called the Ram-Lak filter [6, p. 83] after [51].*

To determine the corresponding convolution kernel, observe that

$$|\nu|\,\mathrm{rect}\left(\frac{\nu}{2\nu_0}\right) = \nu_0\,\mathrm{rect}\left(\frac{\nu}{2\nu_0}\right) - \nu_0\,\mathrm{tri}\left(\frac{\nu}{\nu_0}\right)$$

where $\mathrm{tri}(\cdot)$ was defined in (3.2.12). Thus the convolution kernel is [52]

$$h_{\mathrm{a}}(r) = 2\nu_0^2\,\mathrm{sinc}(2\nu_0 r) - \nu_0^2\,\mathrm{sinc}^2(\nu_0 r), \qquad\text{(3.4.13)}$$

<div style="text-align:right">e,tomo,cbp,kernel</div>
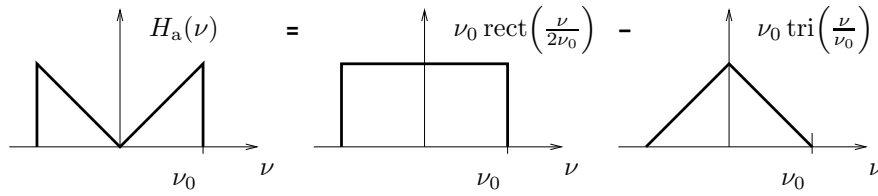
Figure 3.4.5: Frequency response of band-limited ramp filter.
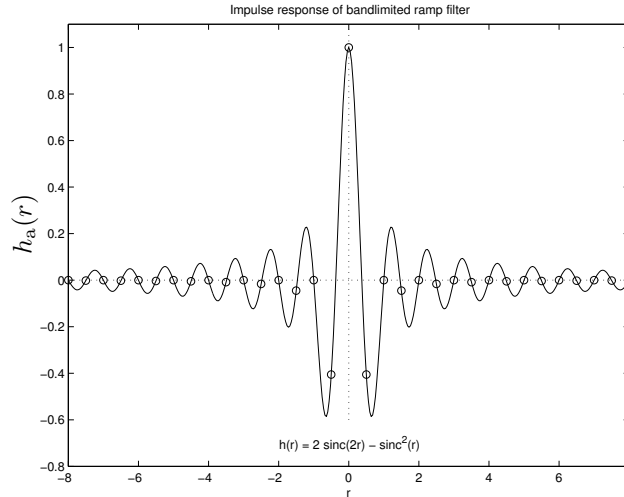
Figure 3.4.6: Convolution kernel for band-limited ramp filter $h_{\mathrm{a}}(r)$ with $\nu_0 = 1$, and the sample values $h[n] = h_{\mathrm{a}}(n/(2\nu_0))$.

as shown in Fig. 3.4.6. The ringing is due to the implicit assumption that the object is band limited. In practice one usually uses an apodization filter $A(\nu)$ that goes to zero gradually to reduce ringing.

In practice, one uses samples of this impulse response. Sampling it using the Nyquist rate yields [5, p. 72]:

$$h[n] = h_{\mathrm{a}}\left(\frac{n}{2\nu_0}\right) = 2\nu_0^2 \operatorname{sinc}(n) - \nu_0^2 \operatorname{sinc}^2(n/2) = \nu_0^2 \begin{cases} 1, & n = 0 \\ 0, & n \text{ even} \\ -1/(\pi n/2)^2, & n \text{ odd}. \end{cases} \qquad (3.4.14)$$

Rarely is ν_0 given in practice, so one assumes that the sampling is adequate, i.e., $\nu_0 = 1/(2\Delta_{\mathrm{R}})$, where Δ_{R} is the radial sample spacing. This approach is preferable to sampling the ramp filter directly in the frequency domain [5, p. 69] [53].

Although the filter (3.4.14) is infinitely long, given a sinogram with a finite number n_{R} of radial samples, we need only to evaluate the filtered sinogram $\check{p}_\varphi(r)$ at those same radial sample locations, so it suffices to compute $h[n]$ for $n = -n_{\mathrm{R}}, \ldots, n_{\mathrm{R}} - 1$ and to zero pad the sinogram radially with n_{R} zeros before computing the FFTs to perform the filtering. When using this discrete-space filter $h[n]$ to approximate the convolution (3.4.9), one should include a scaling factor Δ_{R} to account for $\mathrm{d}r$ in the integral.

Example 3.4.7 *In Example 3.4.5, Fig. 3.4.4 showed the projections of a square after filtering with an ideal ramp filter. Fig. 3.4.4 also shows those same projections when filtered with the rectangularly apodized ramp filter described in Example 3.4.6.*

Example 3.4.8 *For theoretical analysis, an alternative to the rectangular apodization considered in Example 3.4.6 is to use exponential apodization $A(\nu) = \mathrm{e}^{-\varepsilon|\nu|}$, for some small $\varepsilon > 0$. One can verify the following FT pair [54, p. 127]:*

$$h_{\mathrm{a}}(r) = \frac{2(\varepsilon^2 - 4\pi^2 r^2)}{(\varepsilon^2 + 4\pi^2 r^2)^2} \overset{\mathrm{FT}}{\longleftrightarrow} H_{\mathrm{a}}(\nu) = \mathrm{e}^{-\varepsilon|\nu|} |\nu|.$$

Fig. 3.4.7 shows examples of this impulse response. Taking the limit as $\varepsilon \to 0$, yields the following expression for the ramp filter for $r \neq 0$:

$$h_*(r) = \frac{-1}{2\pi^2 r^2},$$

e,tomo,fbp,ramp,hr
(3.4.15)

and a singularity at $r = 0$. (See [55] for rigorous treatment of Fourier transforms of such functions.) This ramp filter satisfies the following scaling property*:*

e,tomo,fbp,ramp,scale

$$h_*(r) = \alpha^2 h_*(\alpha r).$$

(3.4.16)

This is also known as the homogeneity property *[56].*
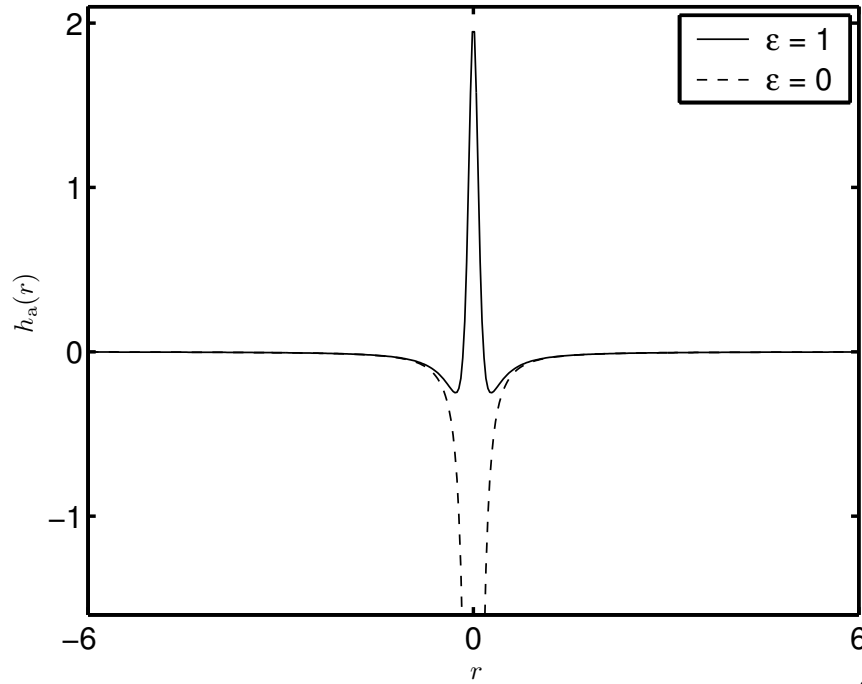
fig˙tomo˙fbp˙ramp˙exp

Figure 3.4.7: Impulse response $h_a(r)$ of ramp filter with exponential apodization.

3.4.7 PSF of the FBP method (s,tomo,fbp,psf)

Apodizing the ramp filter will reduce amplification of high frequency noise, but will also degrade spatial resolution in the reconstructed object. To analyze the effects of apodization, we again turn to the Fourier-slice theorem (3.2.24). By that theorem, multiplying the 1D FT $P_\varphi(\nu)$ of each projection by $A(\nu)$ is equivalent[9] to pre-multiplying the object spectrum by $A(\rho)$, *i.e.*,

$$F(u, v) \mapsto A(\sqrt{u^2 + v^2}) F(u, v).$$

Thus, the reconstructed object $\hat{f}(x, y)$ is a blurred version of the original:

e,tomo,fbp,psf

$$\hat{f}(x, y) = f(x, y) ** h(x, y),$$

(3.4.17)

where

e,tomo,fbp,psf,hankel

$$h(x, y) \overset{\text{2D FT}}{\longleftrightarrow} H(u, v) \triangleq A(\sqrt{u^2 + v^2}).$$

(3.4.18)

Because H is circularly symmetric, so is h; thus $h(r)$ is simply the *Hankel transform* of $H(\rho) = A(\rho)$.

---

[9]Note that for this simple relationship to hold, it is essential that the same apodizer be used for every projection angle φ.

x,tomo,psf,rect **Example 3.4.9** *For the rectangular apodizing window* $A(\nu) = \text{rect}\left(\frac{\nu}{2\nu_0}\right)$, *the corresponding PSF in the image domain would be*

$$h(r) = \nu_0^2 \, \text{jinc}(\nu_0 r) \,.$$

Thus the image would be blurred by a jinc *function, which has large sidelobes that would cause undesirable "ringing."*

x,tomo,psf,gauss **Example 3.4.10** *A popular choice in nuclear medicine is a gaussian window:* $A(\nu) = \exp\left(-\pi(\nu/\nu_0)^2\right)$. *The half-amplitude cutoff frequency* $\nu_{1/2}$ *for this window, i.e., the point where* $A(\nu_{1/2}) = A(0)/2$, *is* $\nu_{1/2} = \nu_0\sqrt{\frac{\log 2}{\pi}} \approx \frac{\nu_0}{2}0.9394 \approx \frac{\nu_0}{2}$. *Because the Hankel transform of a gaussian is gaussian, in the image domain the PSF is*

$$h(r) = \nu_0^2 \exp\left(-\pi(\nu_0 r)^2\right) \,.$$

To find the FWHM of this gaussian, find r *such that* $h(r) = h(0)/2$, *or* $\exp\left(-\pi(\nu_0 r)^2\right) = 1/2$ *so* $\pi(\nu_0 r)^2 = \log 2$. *Thus*

$$FWHM = \frac{2}{\nu_0}\sqrt{\frac{\log 2}{\pi}} \approx \frac{0.9394}{\nu_0} \approx \frac{1}{\nu_0} \approx \frac{1}{2\nu_{1/2}} \,.$$

So for a 5mm FWHM PSF, we would use $\nu_0 = 1/5 = 0.2$ *cycles/cm.*

x,tomo,fbp,other **Example 3.4.11** *Other popular window functions include the following.*
  - *Hann or Hanning:* $A(\nu) = \left[\frac{1}{2} + \frac{1}{2}\cos(\pi\nu/\nu_0)\right]\text{rect}\left(\frac{\nu}{2\nu_0}\right)$
  - *Hamming:* $A(\nu) = \left[0.54 + 0.46\cos(\pi\nu/\nu_0)\right]\text{rect}\left(\frac{\nu}{2\nu_0}\right)$
  - *Generalized Hamming:* $A(\nu) = \left[\alpha + (1-\alpha)\cos(\pi\nu/\nu_0)\right]\text{rect}\left(\frac{\nu}{2\nu_0}\right)$, *for* $\alpha \in [0,1]$
  - *Butterworth:* $A(\nu) = \dfrac{1}{\sqrt{1 + (\nu/\nu_0)^{2n}}}$, *for* $n \geq 0$
  - *Parzen:* $A(\nu) = \begin{cases} 1 - 6(\nu/\nu_0)^2\left(1 - |\nu|/\nu_0\right) & |\nu| \leq \nu_0/2 \\ 2\left(1 - |\nu|/\nu_0\right)^3 & \nu_0/2 \leq |\nu| \leq \nu_0 \\ 0, & \text{otherwise} \end{cases}$
  - *Shepp Logan [57]:* $A(\nu) = \left|\text{sinc}\left(\frac{\nu}{2\nu_0}\right)\right|$ *or* $\left|\text{sinc}\left(\frac{\nu}{2\nu_0}\right)\right|^3$
  - *Modified Shepp Logan:* $A(\nu) = \text{sinc}\left(\frac{\nu}{2\nu_0}\right)\left[0.4 - 0.6\cos(\pi\nu/\nu_0)\right]$

  It is not always easy to find a closed-form expression for the PSF h *that results from apodization. But the general rule of thumb, FWHM* $\approx 1/(2\nu_{1/2})$, *is usually pretty close.*

In light of the result (3.4.17), one might wonder why we apply the window $A(\nu)$ to the projections rather than just smooth (post-filter) the reconstructed image? The main reason is that we have to apply the ramp filter anyway, so we can include $A(\nu)$ essentially for free. In contrast, post-smoothing would require either an "expensive" convolution or a pair of 2D FFTs. However, if one wants to experiment with several different amounts of smoothing, then it is preferable to smooth after a (ramp-filtered) backprojection so that only one backprojection operation is needed.

Summary

We have described three methods for inverting the Radon transform, *i.e.*, for reconstructing a 2D object $f(x,y)$ from its projections $\{p_\varphi(r)\}$:
  - direct Fourier reconstruction (gridding),
  - the backproject-filter (BPF) method (cone filter),
  - the filter-backproject (FBP) method (ramp filter), and its cousin the convolve-backproject (CBP) method.

The derivations of these methods all used the Fourier-slice theorem. These methods would yield identical results for noiseless continuous-space data, but are based on different manipulations of the formulas so they lead to different ways of discretizing and implementing the equations, yielding very different numerical algorithms in practice.

We also analyzed the PSF due to windowing the ramp filter. In practice one must choose the apodizing window to make a suitable compromise between spatial resolution and noise.

Recently, other inversion formulas for the 2D Radon transform have been discovered for objects with compact support, *e.g.*, [58]. These methods include user-selectable parameters that allow one to avoid corrupted or missing regions of the sinogram. An interesting *open problem* is to determine whether the methods could be extended to include some type of statistical weighting.

3.5   Practical backprojection (s,tomo,prac)

In the preceding sections, we have considered the idealized case where there is a continuum of projection views. In practice, sinograms have only a finite number of angular samples, so each of the reconstruction methods described in §3.4 requires modification for practical implementations.

A critical step in both the BPF and FBP reconstruction methods is the *backprojection* operation (3.3.1). Given only a finite number n_φ of projection angles, we must approximate the integral in (3.3.1). Usually the projection angles are uniformly spaced over the interval $[0, \pi)$, *i.e.*,

$$\varphi_i = \left(\frac{i-1}{n_\varphi}\right)\pi, \qquad i = 1, \ldots, n_\varphi.$$

In such cases, the usual approach is to use the following Riemann sum approximation to (3.3.1):

$$f_{\mathrm{b}}(x,y) \approx \frac{\pi}{n_\varphi}\sum_{i=1}^{n_\varphi} p_{\varphi_i}(x\cos\varphi_i + y\sin\varphi_i). \qquad\qquad \text{e,tomo,prac,back} \quad (3.5.1)$$

Whether more sophisticated approximations to this integral would be beneficial is an *open problem*.

There are at least three distinct approaches to implementing (3.5.1): *rotation-based backprojection*, *ray-driven backprojection*, and *pixel-driven backprojection*. If the available projections were continuous functions of the radial argument, then these formulations would be identical. In practice, not only are the projection angles discrete, but also we only have discrete radial samples of $p_\varphi(r)$, as described in (4.3.1). Ignoring noise and blur, we are given the discrete sinogram

$$y_i[n] = p_\varphi(r)\Big|_{\varphi=\varphi_i,\ r=r_c[n]}, \qquad i = 1, \ldots, n_\varphi, \qquad n = 0, \ldots, n_{\mathrm{R}} - 1, \qquad \text{e,tomo,prac,sample} \quad (3.5.2)$$

where the radial sample locations are given by

$$r_c[n] = (n - n_0)\Delta_{\mathrm{R}} \qquad\qquad \text{e,tomo,prac,rcn} \quad (3.5.3)$$

and typically $n_0 = n_{\mathrm{R}}/2$ or $n_0 = (n_{\mathrm{R}} - 1)/2$. For such sinograms, the various backprojection methods can produce different results because they differ in how the equations are discretized.

If the true object f^{true} can be assumed to be appropriately band limited, then its projections will also be band limited (by the Fourier slice theorem), so in principle we could recover p_{φ_i} from $\{y_i[\cdot]\}$ using sinc interpolation:

$$p_{\varphi_i}(r) = \sum_{n=-\infty}^{\infty} y_i[n]\,\mathrm{sinc}\left(\frac{r - r_c[n]}{\Delta_{\mathrm{R}}}\right).$$

In practice this interpolation is inappropriate because: real objects are space limited so they cannot be band limited, sinc interpolation expects an infinite number of samples whereas practical sinograms have only a finite number of samples, and sinc interpolation is computationally impractical. Thus, simpler interpolation methods are used in practice, such as linear interpolation or spline interpolation [59], perhaps combined with oversampling of the FFT used for the ramp filter.

3.5.1   Rotation-based backprojection

We can rewrite the backprojection formula (3.5.1) as follows:

$$f_{\mathrm{b}}(x,y) = \frac{\pi}{n_\varphi}\sum_{i=1}^{n_\varphi} b_i(x,y), \qquad\qquad \text{e,tomo,prac,back,ray} \quad (3.5.4)$$

where the backprojection of the ith view is given by:

$$b_i(x, y) = p_{\varphi_i}(x \cos\varphi_i + y \sin\varphi_i).$$

We can also write $b_i = \boldsymbol{\mathcal{P}}_{\varphi_i}^* p_{\varphi_i}$, where $\boldsymbol{\mathcal{P}}_{\varphi_i}^*$ is defined in (4.2.4). This adjoint maps the ith 1D projection back into a 2D object by "smearing" that projection along the angle φ_i. In this approach, we form temporary images by backprojecting each view and accumulating the sum of those temporary images.

To better understand $b_i(x, y)$, note that when $i = 1$ we have $\varphi = 0$, so

$$b_1(x, y) = p_0(x),$$

which is just a 2D version of the function $p_0(x)$.

Mat *For radially-sampled sinograms, implementing $\boldsymbol{\mathcal{P}}_0^*$ is trivial[10] (e.g., in MATLAB), simply replicate the first row of the sinogram (a vector) to make a matrix. For other angles, perform the following steps.*
- *Replicate the ith sinogram row to make an image, as if it were the $\varphi = 0$ case*
- *Use* `imrotate` *to rotate that image counter clockwise by φ. This rotation will require an interpolation method, such as bilinear interpolation or a more precise spline approach [60].*
- *Accumulate these rotated images over all angles, as described in (3.5.4).*

In this approach, the "outer loop" is over projection angles. The first step (replication) inherently "accounts" for discrete radial samples.

The rotation approach is easily implemented but can be somewhat slow because rotation is a fairly expensive operation.

3.5.2 Ray-driven backprojection

For *ray-driven backprojection*, one loops through all the rays and for each ray one interpolates $y_i[n]$ onto the pixels whose centers are nearest to the ray $\mathcal{L}(r_c[n], \varphi_i)$, as defined in (3.2.2). Although this approach is somewhat popular for *forward projection*, it can produce significant artifacts when used for back projection, so will not be considered further here. Fig. 3.3.1 somewhat illustrates the approach.

When radial sample spacing equals image sample spacing, ray-driven backprojection is equivalent to rotation-based backprojection [61].

3.5.3 Pixel-driven backprojection

For image display, we need to compute $f_b(x, y)$ only on a finite grid of pixel coordinate pairs $\{(x_j, y_j) : j = 1, \ldots, n_p\}$. For *pixel-driven backprojection*, we loop over the (x_j, y_j) pairs of interest and evaluate (3.5.1) for each of the grid points, thereby filling up an image matrix. To implement, the outer loop is over pixel index j and the inner loop is over angles φ_i. In essence, for each pixel we are summing along the corresponding sinusoid (illustrated in Fig. 3.2.4) in the sinogram.

However, the radial argument $x_j \cos\varphi_i + y_j \sin\varphi_i$ in (3.5.1) rarely exactly equals one of the radial sample locations $r_c[n]$ shown in (3.5.2). Therefore, radial interpolation is required for pixel-driven backprojection. The usual approach is *linear interpolation* which is equivalent mathematically to the following approximation:

$$p_{\varphi_i}(r) \approx \sum_n y_i[n] \operatorname{tri}\left(\frac{r - r_c[n]}{\Delta_{\mathrm{R}}}\right), \qquad (3.5.5)$$

where the *unit triangle function* is denoted:

$$\operatorname{tri}(t) = \begin{cases} 1 - |t|, & |t| \leq 1, \\ 0, & \text{otherwise.} \end{cases}$$

Although (3.5.5) is mathematically correct and is useful for theoretical analysis, it poorly conveys how one would implement linear interpolation in practice. Because support of the function $\operatorname{tri}(t)$ is two sample units, for any given r,

---

[10]This method assumes that $n_0 = (n_{\mathrm{R}} - 1)/2$, *i.e.*, that the center of the image projects onto the center of each projection. It furthermore assumes that the desired pixel size equals Δ_{R}. Otherwise a more complicated approach is needed.

only two terms in the sum in (3.5.5) are possibly nonzero. An alternative expression is

$$
\begin{aligned}
p_{\varphi_i}(r) &\approx y_i[n(r)] \operatorname{tri}\left(\frac{r - r_c[n(r)]}{\Delta_{\mathrm{R}}}\right) + y_i[n(r) + 1] \operatorname{tri}\left(\frac{r - r_c[n(r) + 1]}{\Delta_{\mathrm{R}}}\right) \\
&= y_i[n(r)] \left(1 - \frac{r - r_c[n(r)]}{\Delta_{\mathrm{R}}}\right) + y_i[n(r) + 1]\left(\frac{r - r_c[n(r)]}{\Delta_{\mathrm{R}}}\right),
\end{aligned}
$$

where we define

$$
n(r) \triangleq \lfloor r/\Delta_{\mathrm{R}} + n_0 \rfloor.
$$

Other interpolators, such as an oversampled FFT or spline functions are also used [59].

3.5.4 Interpolation effects

Generalizing (3.5.5), suppose that we use an interpolation method of the form:

$$
\hat{p}_{\varphi_i}(r) = \sum_n y_i[n]\, h\left(\frac{r - r_c[n]}{\Delta_{\mathrm{R}}}\right)
$$

for some interpolation kernel $h(\cdot)$. Suppose furthermore that $p_{\varphi}(r)$ is band limited with maximum frequency less than $\frac{1}{2\Delta_{\mathrm{R}}}$. Then it follows from (3.5.2) and the sampling theorem that (ignoring noise):

$$
\hat{P}_{\varphi_i}(\nu) = \begin{cases} P_{\varphi_i}(\nu)\, H(\nu), & |\nu| < \frac{1}{2\Delta_{\mathrm{R}}} \\ 0, & \text{otherwise.} \end{cases}
$$

For example, when h is the linear interpolator in (3.5.5), we have $H(\nu) = \Delta_{\mathrm{R}} \operatorname{sinc}^2(\Delta_{\mathrm{R}}\nu)$, which is strictly positive for $|\nu| < \frac{1}{2\Delta_{\mathrm{R}}}$. Therefore, while we are applying the ramp filter $|\nu|$ in the discretized version of (3.4.2), we can also apply the *inverse filter* $1/H(\nu)$ to compensate for the effects of interpolation [62, eqn. (45)] [59, 63].

Summary

Pixel-driven, rotation-based, and ray-driven backprojection are all used in practice, depending on number of samples, sample spacing, etc. The formulations are exactly identical in continuous space, but can yield slightly different results when discretized.

3.6 Sinogram restoration (s,tomo,restore)

Because a sinogram $p_{\varphi}(r)$ has two coordinates (r and φ), one can display it as a 2D picture or even treat it as a 2D "image" and apply any number of image processing methods to it. Numerous linear and nonlinear filters have been applied to sinograms in an attempt to reduce noise [64–84] to extrapolate missing data [85–88] and to compensate for detector blur [89–96] and/or SPECT attenuation [97–100]. Some of these methods can even be called "statistical" methods because they include measurement noise models. Problem 3.12 explores an approach based on B-splines.

A typical linear approach for a system with shift-invariant blur having frequency response $B(\nu)$ would be to use a *Wiener filter* as the apodizing filter $A(\nu)$ in (3.4.8) as follows

$$
A(\nu) = \frac{B^*(\nu)}{|B(\nu)|^2 + S_p(\nu)},
$$

where $S_p(\nu)$ is some model for the power spectral density of $p_{\varphi}(r)$ under the (questionable) assumption that $p_{\varphi}(r)$ is a WSS random process.

Nonlinear sinogram preprocessing methods, including classical methods based on view-adaptive Wiener filters [101] and contemporary approaches like wavelet-based denoising [102], have the potential to reduce noise more than linear methods with less degradation of spatial resolution. However, when a nonlinear sinogram filtering method is combined with the linear FBP reconstruction method the resulting spatial resolution properties can be quite unusual. It is the author's view that nonlinear processing is more safely performed in the image domain, *e.g.*, by nonquadratic edge-preserving regularization, instead of in the sinogram domain.

3.7   Sampling considerations (s,tomo,samp)

In practice one can only acquire a finite number of radial and angular samples, due to constraints such as cost and time. This section describes considerations in choosing the radial and angular sampling.

3.7.1   Radial sampling

The radial sample spacing, Δ_{R}, should be determined by the spatial resolution (in the radial direction) of the tomographic scanning instrument. The FWHM of the system radial resolution is a function of the detector width, the source size in X-ray imaging, etc. The radial detector response (*e.g.*, a rectangular function for square detector elements) generally is not exactly band-limited, so Nyquist sampling theory can provide only general guidance. A practical rule-of-thumb is to choose (if possible): $\Delta_{\mathrm{R}} = \text{FWHM}/2$. Then the number of radial samples should be determined to cover the desired FOV by choosing: $n_{\mathrm{R}} = \text{FOV}/\Delta_{\mathrm{R}}$. See §4.3.9 for Fourier analysis of aliasing due to radial sampling.

3.7.2   Angular sampling

For a given FOV and radial sampling, what should the angular sampling Δ_{φ} be? If we have n_{R} radial samples spaced by Δ_{R}, then in the Fourier domain (of the 2D DFT), the corresponding spatial frequencies are spaced by $\Delta_{\nu} = 1/(n_{\mathrm{R}}\Delta_{\mathrm{R}})$. It is natural to choose the angular sampling so as to ensure that all samples in the 2D Fourier domain are separated by no more than this amount.
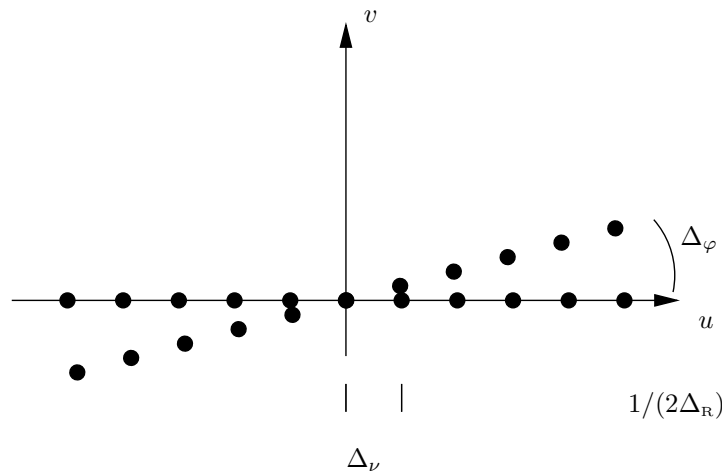
fig,tomo,ang,sample

Figure 3.7.1: Angular sampling considerations.

Considering Fig. 3.7.1, the appropriate angular spacing is $\Delta_{\varphi} = \dfrac{\Delta_{\nu}}{1/(2\Delta_{\mathrm{R}})} = 2/n_{\mathrm{R}}$. So the total number of angles over $180°$ should be

$$\boxed{n_{\varphi} = \frac{\pi}{\Delta_{\varphi}} = \frac{\pi}{2}n_{\mathrm{R}}.}$$

In practice often somewhat fewer angular samples are used, but usually $n_{\varphi} \approx n_{\mathrm{R}}$. The reason for using fewer than $\pi n_{\mathrm{R}}/2$ angular samples is that often in real systems there is blur in the radial direction so the spatial resolution is somewhat lower than that implied by just the radial sampling, *i.e.*, the radial sampling may be a little finer than necessary from a strict Nyquist perspective. However, we rarely use Nyquist (sinc) reconstruction, but rather only linear interpolation, so a little "oversampling" is reasonable. Inadequate angular sampling can lead to significant aliasing artifacts. On the other hand, for the FBP reconstruction method, the computation time is directly proportional to the number of angles.

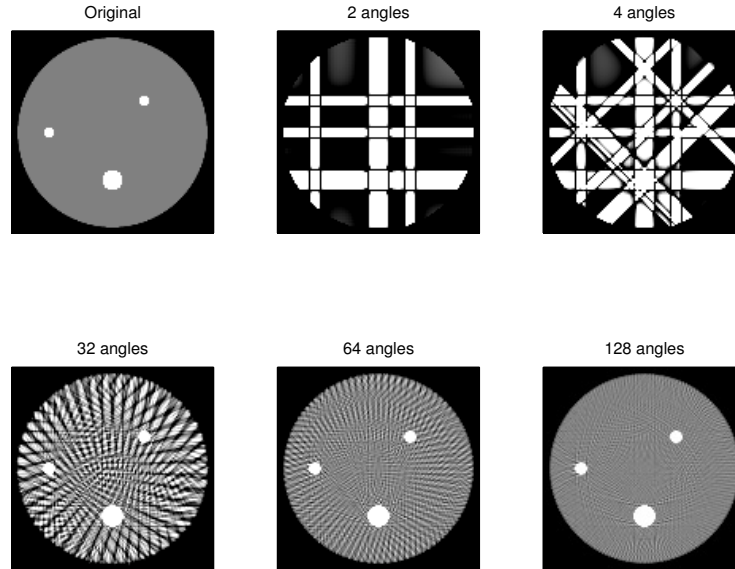**Example 3.7.1** *Fig. 3.7.2 illustrates the effects of angular undersampling.*

Figure 3.7.2: Illustration of the effects of angular undersampling on image quality for FBP reconstruction. The image is 128×128, and the true values of the digital phantom are 1 in the background disk and 8 in the small disks. The grayscale display is windowed from 0.5 to 1.5 to enhance the visibility of the artifacts.

3.8 Linogram reconstruction (s,tomo,lino)

For tomographic imaging systems with certain geometries involving flat detectors, it can be convenient to use an alternative coordinate system of the form

$$
\begin{aligned}
p^{\mathrm{EW}}(s, \beta) &= \frac{1}{\sqrt{1 + \beta^2}}\, p_{\arctan(\beta)}\left(\frac{s}{\sqrt{1 + \beta^2}}\right) \\
p^{\mathrm{NS}}(s, \beta) &= \frac{1}{\sqrt{1 + \beta^2}}\, p_{\pi/2 + \arctan(\beta)}\left(\frac{s}{\sqrt{1 + \beta^2}}\right),
\end{aligned}
\tag{3.8.1}
$$

for $|\beta| \leq 1$. This is called a *linogram* [7, 37, 103–105], because in this coordinate system the projection of a point source is a straight line.

Taking the 1D Fourier transform of $p^{\mathrm{EW}}(s, \beta)$ and $p^{\mathrm{NS}}(s, \beta)$ along s and applying the *Fourier slice theorem* yields the Fourier relationships:

$$
\begin{aligned}
P_{\varphi}^{\mathrm{EW}}(\nu) &= \sqrt{1 + \beta^2}\, P_{\arctan(\beta)}\left(\sqrt{1 + \beta^2}\,\nu\right) = F(\nu, \beta\nu) \\
P_{\varphi}^{\mathrm{NS}}(\nu) &= \sqrt{1 + \beta^2}\, P_{\pi/2 + \arctan(\beta)}\left(\sqrt{1 + \beta^2}\,\nu\right) = F(-\beta\nu, \nu).
\end{aligned}
\tag{3.8.2}
$$

So the 1D Fourier transform of linogram data corresponds to samples of the object spectrum $F(u, v)$ along lines with slope β or $1/\beta$. In particular, for a projection at slope β, if the linogram data has n_{s} equally spaced samples along s with spacing Δ_{s}, then the corresponding samples of the object spectrum $F(u, v)$ in 2D Fourier space along the line at slope β are spaced by $\sqrt{1 + \beta^2}/(n_{\mathrm{s}}\Delta_{\mathrm{s}})$, corresponding to the *pseudo-polar* grid shown in Fig. 3.8.1. Using this sampling pattern, one can develop *direct Fourier reconstruction* methods for linogram data akin to §3.4.1, *e.g.*, [106, 107]. See Chapter 6 for more options. The linogram concept has been generalized to higher dimension data, called *planogram* reconstruction [108–111].

By equating φ with $\arctan(\beta)$ or $\pi + /2 + \arctan(\beta)$, one can show that $\sqrt{1 + \beta^2} = \frac{1}{\max(|\cos\varphi|, |\sin\varphi|)}$. Therefore the radial sample spacing in (3.8.1) is the same as that of *Mojette sampling* described in §25.2.6. The primary difference between linogram and Mojette sampling is in the angular sampling.
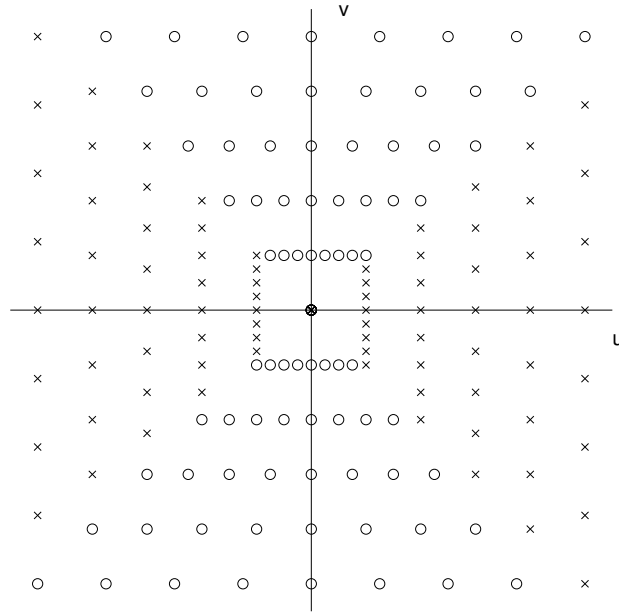
Figure 3.8.1: Illustration of pseudo-polar grid in 2D Fourier space associated with linogram sampling. The cross marks and circles correspond to the $P_\varphi^{\mathrm{EW}}(\nu)$ samples and the $P_\varphi^{\mathrm{NS}}(\nu)$ samples respectively.

s,tomo,fan
3.9 2D fan beam tomography (s,tomo,fan)

The preceding sections have focused on case of 2D parallel-beam projections. Although 1st-generation X-ray CT scanners did correspond to that geometry, many contemporary tomographic imaging systems have *fan beam* geometries, including commercial X-ray CT scanners and some collimators for SPECT systems. For hypothetical continuous measurements, one could transform fan-beam projections into parallel-beam projections by a simple change of variables. For discrete, noisy measurements, *rebinning* fan-beam measurements into parallel-beam projections requires an interpolation operation that could degrade spatial resolution. To avoid such rebinning, one can derive analytical reconstruction methods directly in terms of the fan-beam coordinates, as described below.

Fig. 3.9.1 illustrates the fan-beam geometry that will be considered here. Because it can be challenging mechanically to ensure that the line between the X-ray source and the midpoint of the detector passes through the exact center of rotation, we allow an offset r_{off} between that line and the center [112]. Let P denote the point along that line that intersects the circle of radius r_{off} centered at the rotation isocenter. $D_{0\mathrm{d}}$ denotes the distance from the point P to the detector, $D_{\mathrm{s}0}$ denotes the distance from the X-ray source to P, and D_{fs} denotes the distance from the focal point of the detector arc to the X-ray source. Define $D_{\mathrm{sd}} \triangleq D_{0\mathrm{d}} + D_{\mathrm{s}0}$ to be the total distance from the X-ray source to the center of the detector. This formulation allows the detector focal point to differ from the X-ray source location to encompass a variety of system configurations. For flat detectors, $D_{\mathrm{fs}} = \infty$. For third-generation X-ray CT systems, $D_{\mathrm{fs}} = 0$. For fourth generation X-ray CT systems, $D_{\mathrm{fs}} = -D_{\mathrm{s}0}$.

In our notation, the distances $D_{0\mathrm{d}}$ and $D_{\mathrm{s}0}$ are constants, rather than being functions of angle β. Generalizations exist to allow non-circular source trajectories [113].

Let $s \in [-s_{\max}, s_{\max}]$ denote the (signed) *arc length* along the detector, with $s = 0$ corresponding the detector center. Arc length is the natural parameterization for detector elements that are spaced equally along the detector. (For a flat detector with $D_{\mathrm{fs}} = \infty$, the arc length s is simply the position along the detector.) The various angles have the following relationships:

$$\alpha(s) = \frac{s}{D_{\mathrm{fd}}}, \qquad \gamma(s) = \arctan\left(\frac{D_{\mathrm{fd}} \sin\alpha(s)}{D_{\mathrm{fd}} \cos\alpha(s) - D_{\mathrm{fs}}}\right),$$

e,tomo,fan,alf,gam
(3.9.1)

where $D_{\mathrm{fd}} \triangleq D_{\mathrm{fs}} + D_{\mathrm{sd}}$. The two most important cases are

$$\gamma(s) = \begin{cases} s/D_{\mathrm{sd}}, & D_{\mathrm{fs}} = 0 \quad \text{(equiangular)} \\ \arctan(s/D_{\mathrm{sd}}), & D_{\mathrm{fs}} = \infty \quad \text{(equidistant)}. \end{cases}$$

e,tomo,fan,tan,gam
(3.9.2)

Figure 3.9.1: Illustration of fan beam geometry.

The function $\gamma(s)$ is anti-symmetric and increasing and the (inverse) relationship between γ and s is:

$$s = \begin{cases} D_{\mathrm{fd}}\left[\gamma - \arcsin\left(\frac{D_{\mathrm{fs}}}{D_{\mathrm{fd}}}\sin\gamma\right)\right], & 0 \le D_{\mathrm{fs}} < \infty \\ D_{\mathrm{sd}}\tan\gamma, & D_{\mathrm{fs}} = \infty. \end{cases}$$

<div style="text-align:right">e,tomo,fan,gam,inv
(3.9.3)</div>

The ray corresponding to angle β and detector element s is

$$\mathcal{L}(s,\beta) = \{(x,y) : x\cos\varphi(s,\beta) + y\sin\varphi(s,\beta) = r(s)\},$$

<div style="text-align:right">e,tomo,fan,Ray
(3.9.4)</div>

where

$$\begin{aligned} \varphi(s,\beta) &\triangleq \beta + \gamma(s) \\ r(s) &\triangleq D_{\mathrm{s0}}\sin\gamma(s) + r_{\mathrm{off}}\cos\gamma(s) \\ &= \sqrt{D_{\mathrm{s0}}^2 + r_{\mathrm{off}}^2}\,\sin(\gamma(s) + \beta_{\mathrm{off}}), \end{aligned}$$

<div style="text-align:right">e,tomo,fan,r,ang
(3.9.5)</div>

where we define $\beta_{\mathrm{off}} \triangleq \angle(D_{\mathrm{s0}}, r_{\mathrm{off}})$. Unlike in our analysis of parallel-beam tomography, here the range of r is limited inherently by the position of the X-ray source and the extent of the detector:

$$|r(s)| \le r_{\max} \triangleq D_{\mathrm{s0}}\sin\gamma_{\max},$$

<div style="text-align:right">e,tomo,fan,rmax
(3.9.6)</div>

where $\gamma_{\max} \triangleq \gamma(s_{\max})$ and $s_{\max}$ is half of the total arc length of the detector. The radius $r_{\max}$ defines the circular *field of view* of the imaging system: the subset of the plane that is measured completely. (We assume that $D_{\mathrm{0d}} \ge r_{\max}$, because otherwise even the detector center would limit the field of view.) The angle $2\gamma_{\max}$ is called the *fan angle*. A typical clinical CT scanner has $D_{\mathrm{sd}} \approx 95$ cm, $s_{\max} \approx 45$ cm, so $\gamma_{\max} \approx \pi/6$.

Fig. 3.9.2 illustrates the sampling (3.9.5) associated with the fan-beam geometry, before and after the values of (r, φ) are collapsed to the range described in (3.2.8).

The line-integral projection $p(s,\beta)$ of f along $\mathcal{L}(s,\beta)$ is[11]:

$$\begin{aligned} p(s,\beta) &= \int_{\mathcal{L}(s,\beta)} f(x,y)\,\mathrm{d}\ell \\ &= \iint f(x,y)\,\delta(x\cos\varphi(s,\beta) + y\sin\varphi(s,\beta) - r(s))\,\mathrm{d}x\,\mathrm{d}y, \end{aligned}$$

<div style="text-align:right">e,tomo,fan,psb
(3.9.7)</div>

---

[11]Practically speaking, the integral should be restricted to the field of view: $\sqrt{x^2 + y^2} \le r_{\max}$, but this restriction would complicate analysis by introducing a shift variance into the problem, so we ignore it.
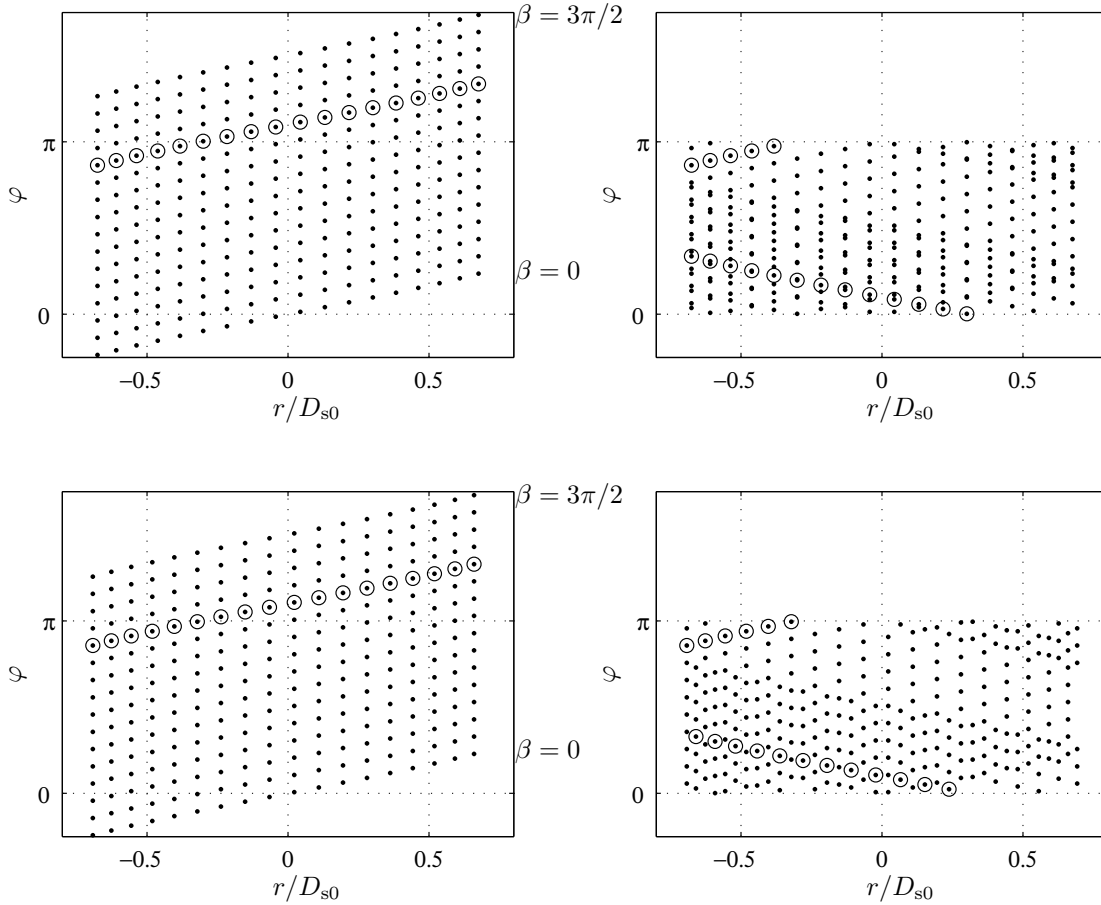
Figure 3.9.2: Left: (r, φ) coordinates for equiangular fan-beam samples based directly on (3.9.5). The fan angle is $2\gamma_{\max} = \pi/3$. Right: after converting φ to the range $[0, \pi)$ using the periodicity property (3.2.19). Top: for equally spaced samples in s symmetrical around $s = 0$. Bottom: for equally spaced samples in s with quarter-detector offset. The samples for one particular value of β are circled for illustration.

for $|s| \leq s_{\max}$ and $0 \leq \beta < \beta_{\max}$. We assume $\beta_{\max} \geq \pi + 2\gamma_{\max}$ to ensure complete sampling. By (3.9.5), fan-beam projections satisfy the following general symmetry property:

$$p\big(\gamma^{-1}(-\gamma(s) - 2\beta_{\mathrm{off}}), \ \beta \pm \pi + 2\gamma(s) + 2\beta_{\mathrm{off}}\big) = p(s, \beta). \qquad \substack{\text{e,tomo,fan,sym} \\ (3.9.8)}$$

In particular, if $D_{\mathrm{fs}} = 0$, then

$$p(-s - 2D_{\mathrm{sd}}\beta_{\mathrm{off}}, \ \beta \pm \pi + 2s/D_{\mathrm{sd}} + 2\beta_{\mathrm{off}}) = p(s, \beta). \qquad \substack{\text{e,tomo,fan,sym,Dfs=0} \\ (3.9.9)}$$

Alternatively, if $\beta_{\mathrm{off}} = 0$, then

$$p(-s, \ \beta \pm \pi + 2\gamma(s)) = p(s, \beta). \qquad \substack{\text{e,tomo,fan,sym,boff=0} \\ (3.9.10)}$$

The reconstruction problem is to estimate f from the fan-beam projections $\{p(s, \beta)\}$.

s,tomo,fan,rebin

3.9.1 Fan-parallel rebinning methods (s,tomo,fan,rebin)

In continuous space, to *rebin* from fan-beam to parallel-beam coordinates requires a simple change of variables based on (3.9.5). In the usual case where $r_{\mathrm{off}} = 0$, we can express the parallel-beam projections in terms of the fan-beam projections using the following relationship:

$$p_\varphi(r) = p(s, \beta)\Big|_{s=s(r), \ \beta=\beta(r,\phi)} = p\big(\gamma^{-1}(\arcsin(r/D_{\mathrm{s0}})), \phi - \arcsin(r/D_{\mathrm{s0}})\big), \qquad \substack{\text{e,tomo,fan,rebin} \\ (3.9.11)}$$

where γ^{-1} is defined by (3.9.3). For sampled measurements, usually one first performs 1D interpolation along the source position using the relationship $\phi = \beta + \gamma$. Then one performs 1D interpolation along the detector by relating r and s. When the s samples include a *quarter detector offset*, then the radial sampling can be improved by a factor of two, at least for 360° scans, as illustrated in Fig. 3.9.2.

IRT *See* `rebin_fan2par.m`.

s,tomo,fan,fbp

3.9.2 The filter-backproject (FBP) approach for 360° scans (s,tomo,fan,fbp)

This section derives filter-backproject methods for the fan-beam geometry shown in Fig. 3.9.1, including the case of displaced center of rotation [112]. We focus on the case of 360° rotation of the X-ray source and detector [5, p. 77].

We start by rewriting the parallel-ray FBP formula (3.4.11) for the case of 360° rotation:

$$f(x,y) = \frac{1}{2} \int_0^{2\pi} \int p_\varphi(r)\, h_*(x\cos\varphi + y\sin\varphi - r)\, \mathrm{d}r\, \mathrm{d}\varphi, \qquad \text{(3.9.12)}$$

<div align="right">e,tomo,fan,fbp,360</div>

where $h_*(\cdot)$ denotes the ramp filter in (3.4.15) with 1D Fourier transform $H_*(\nu) = |\nu|$.

Now change to fan-beam coordinates by making the transformation of variables $r = r(s)$, $\varphi = \varphi(s,\beta)$, defined in (3.9.5). The Jacobian matrix is

$$\begin{bmatrix} \frac{\partial}{\partial s} r(s) & \frac{\partial}{\partial \beta} r(s) \\ \frac{\partial}{\partial s} \varphi(s,\beta) & \frac{\partial}{\partial \beta} \varphi(s,\beta) \end{bmatrix} = \begin{bmatrix} [D_{s0}\cos\gamma(s) - r_{\text{off}}\sin\gamma(s)]\,\dot\gamma(s) & 0 \\ \dot\gamma(s) & 1 \end{bmatrix}, \qquad \text{(3.9.13)}$$

<div align="right">e,tomo,fan,J</div>

the determinant of which is

$$J(s) \triangleq |D_{s0}\cos\gamma(s) - r_{\text{off}}\sin\gamma(s)|\,|\dot\gamma(s)|. \qquad \text{(3.9.14)}$$

<div align="right">e,tomo,fan,detJ</div>

The reconstruction formula becomes

$$\begin{aligned} f(x,y) &= \frac{1}{2}\int_0^{2\pi}\int p(s,\beta)\, h_*(x\cos\varphi(s,\beta) + y\sin\varphi(s,\beta) - r(s))\, J(s)\, \mathrm{d}s\, \mathrm{d}\beta \\ &= \frac{1}{2}\int_0^{2\pi}\int p(s,\beta)\, J(s)\, h_*(x\cos(\beta + \gamma(s)) + y\sin(\beta + \gamma(s)) - D_{s0}\sin\gamma(s) - r_{\text{off}}\cos\gamma(s))\, \mathrm{d}s\, \mathrm{d}\beta. \end{aligned}$$

Although this expression is a fan-beam reconstruction formula, it is inconvenient for practical use; the challenge is to manipulate it so that it has a filter-backproject form.

Using trigonometric identities, one can simplify the argument of h_* above as follows:

$$x\cos(\beta + \gamma) + y\sin(\beta + \gamma) - D_{s0}\sin\gamma - r_{\text{off}}\cos\gamma = L(x,y,\beta)\sin(\gamma'(x,y,\beta) - \gamma), \qquad \text{(3.9.15)}$$

<div align="right">e,tomo,fan,fbp,h,arg</div>

where

$$\begin{aligned} x_\beta &\triangleq x\cos\beta + y\sin\beta \\ y_\beta &\triangleq -x\sin\beta + y\cos\beta \\ L(x,y,\beta) &\triangleq \sqrt{(D_{s0} - y_\beta)^2 + (x_\beta - r_{\text{off}})^2} \\ \gamma'(x,y,\beta) &\triangleq \tan^{-1}\left(\frac{x_\beta - r_{\text{off}}}{D_{s0} - y_\beta}\right). \end{aligned} \qquad \text{(3.9.16)}$$

<div align="right">e,tomo,fan,L,gam</div>

Defining s' by $\gamma' = \gamma(s')$, using (3.9.15), and applying the *scaling property* of the ideal ramp filter[12] (3.4.16) leads to the following form for the fan-beam reconstruction formula:

$$\begin{aligned} f(x,y) &= \frac{1}{2}\int_0^{2\pi}\int p(s,\beta)\, J(s)\, h_*(L(x,y,\beta)\sin(\gamma'(x,y,\beta) - \gamma(s)))\, \mathrm{d}s\, \mathrm{d}\beta \\ &= \frac{1}{2}\int_0^{2\pi}\int p(s,\beta)\, J(s)\left(\frac{s'(x,y,\beta) - s}{L(x,y,\beta)\sin(\gamma'(x,y,\beta) - \gamma(s))}\right)^2 h_*(s'(x,y,\beta) - s)\, \mathrm{d}s\, \mathrm{d}\beta. \end{aligned}$$

---

[12]Zeng *et al.* note that using this property leads to nonuniform image noise variance in practice [56] and propose an alternative approach based on Hilbert transforms [114].

For certain special fan-beam geometries, we can express the $\sin$ term above as follows:

$$\sin(\gamma'(x,y,\beta) - \gamma(s)) = W_2(x,y,\beta)\, W_1(s)\, W_0(s'(x,y,\beta) - s),$$

<div align="right">e,tomo,fan,fbp,sin
(3.9.17)</div>

for some geometry-dependent weighting functions W_0, W_1, and W_2. For such geometries, the fan-beam reconstruction formula simplifies as follows:

$$f(x,y) = \frac{1}{2}\int_0^{2\pi} \frac{1}{W_2^2(x,y,\beta)\, L^2(x,y,\beta)} \left[\int p(s,\beta)\, \frac{J(s)}{W_1^2(s)}\, g(s'(x,y,\beta) - s)\, \mathrm{d}s \right] \mathrm{d}\beta,$$

where we define the following modified ramp filter:

$$g(s) \triangleq \left(\frac{s}{W_0(s)} \right)^2 h_*(s).$$

<div align="right">e,tomo,fan,ramp,gen
(3.9.18)</div>

Thus, the fan-beam FBP method uses the following three steps.
- Step 1. Compute *weighted* projections:

$$\tilde{p}(s,\beta) \triangleq p(s,\beta)\, \frac{J(s)}{W_1^2(s)}.$$

<div align="right">e,tomo,fan,psb,weight
(3.9.19)</div>

- Step 2. Filter those weighted projections using the modified ramp filter:

$$\check{p}(s,\beta) \triangleq \tilde{p}(s,\beta) * g(s), \quad \forall \beta.$$

- Step 3. Perform a *weighted* backprojection of those filtered projections:

$$f(x,y) = \frac{1}{2}\int_0^{2\pi} \frac{1}{W_2^2(x,y,\beta)\, L^2(x,y,\beta)}\, \check{p}(s'(x,y,\beta),\beta)\, \mathrm{d}\beta.$$

<div align="right">e,tomo,fan,fbp,wtd,back
(3.9.20)</div>

This three-step procedure is quite practical and has been used routinely in commercial X-ray CT systems.

The existence of this efficient FBP approach hinges on whether a factorization of the form (3.9.17) exists. Besson has shown that there are exactly four fan-beam geometries for which this is possible [113]. Fortunately, two of the four cases are the important ones described in (3.9.2). Somewhat unfortunately, the 4th generation CT scanner geometry is *not* one of the four cases, although most commercial CT scanners are 3rd generation.

3.9.2.1 Equiangular case

The case where $D_{\mathrm{fs}} = 0$ corresponds to 3rd-generation X-ray CT systems using an arc detector, called the *equiangular case* [115]. In this case, $\gamma(s) = s/D_{\mathrm{sd}}$, so we factor the $\sin$ term in (3.9.17) as follows:

$$\sin(\gamma'(x,y,\beta) - \gamma(s)) = W_2\, W_0(s'(x,y,\beta) - s),$$

$$\text{where } W_2 = \frac{1}{D_{\mathrm{sd}}}, \quad W_0(s) = D_{\mathrm{sd}} \sin\left(\frac{s}{D_{\mathrm{sd}}} \right), \quad s'(x,y,\beta) = D_{\mathrm{sd}}\, \gamma'(x,y,\beta),$$

with $W_1 = 1$. Thus the modified ramp filter (3.9.18) is

$$g(s) = \left(\frac{s/D_{\mathrm{sd}}}{\sin(s/D_{\mathrm{sd}})} \right)^2 h_*(s).$$

<div align="right">e,tomo,fan,ramp,ea
(3.9.21)</div>

Because $\dot{\gamma}(s) = 1/D_{\mathrm{sd}}$, the projection weighting in (3.9.19) simplifies to

$$\frac{J(s)}{W_1^2} = J(s) = \frac{1}{D_{\mathrm{sd}}} \left| D_{\mathrm{s0}} \cos\frac{s}{D_{\mathrm{sd}}} - r_{\mathrm{off}} \sin\frac{s}{D_{\mathrm{sd}}} \right| \approx \frac{D_{\mathrm{s0}}}{D_{\mathrm{sd}}} \cos\frac{s}{D_{\mathrm{sd}}},$$

<div align="right">e,tomo,fan,J˙w1w1,ea
(3.9.22)</div>

and the backprojection weighting in (3.9.20) is

$$\frac{1}{W_2^2\, L^2(x,y,\beta)} = \frac{D_{\mathrm{sd}}^2}{L^2(x,y,\beta)} = \frac{D_{\mathrm{sd}}^2}{(D_{\mathrm{s0}} - y_\beta)^2 + (x_\beta - r_{\mathrm{off}})^2}.$$

<div align="right">e,tomo,fan,fbp,w2,ea
(3.9.23)</div>

Note that as $D_{s0} \to \infty$, *i.e.*, as the rays become more parallel, the modified ramp filter approaches the usual ramp filter, and the projection and backprojection weightings approach unity, as expected for the parallel-ray case.

For practical implementation the filter must be band-limited and sampled. Combining (3.9.21) with (3.4.14) for $h_a(r)$, the necessary filter samples are

$$h[n] = \begin{cases} \dfrac{1}{4\Delta_s^2}, & n = 0 \\ 0, & n \text{ even} \\ \dfrac{-1}{[\pi D_{sd} \sin(n\Delta_s/D_{sd})]^2}, & n \text{ odd}, \end{cases} \qquad \text{e,tomo,fan,ramp,ea,sample} \atop (3.9.24)$$

where Δ_s denotes the detector element spacing. (Note that there is an error in [5, eqn. (96)].)

There is a subtle issue in the above derivation [56, 114]. We first applied the scaling property of the ramp filter, continued the derivation, and then eventually considered a band-limited ramp filter (3.9.24). If we had considered the band-limiting effect first, which might be more appropriate for sampled data, then the scaling property would not hold exactly. It has been stated that this practice "results in a nonstationary cutoff frequency in the image" [56, 114]. Nevertheless, it is used widely.

IRT *See* `fbp_ramp.m`.

IRT *See* `fbp_fan_arc.m`.

3.9.2.2 Equidistant case

The case where $D_{fs} = \infty$ corresponds to a flat detector, called the *equidistant case* [116]. In this case, $\gamma(s) = \arctan(s/D_{sd})$ and (with some trigonometric identities) we factor the sin term in (3.9.17) as follows:

$$\sin(\gamma' - \gamma) = \sin\gamma'\cos\gamma - \sin\gamma\cos\gamma' = \cos\gamma'\cos\gamma\,(\tan\gamma' - \tan\gamma) = \cos\gamma' \frac{D_{sd}}{\sqrt{D_{sd}^2 + s^2}} \frac{s' - s}{D_{sd}},$$

where $s'(x,y,\beta) = D_{sd}\tan\gamma'(x,y,\beta)$, or equivalently:

$$W_2 = \frac{\cos\gamma'(x,y,\beta)}{D_{sd}}, \quad W_1 = \frac{D_{sd}}{\sqrt{D_{sd}^2 + s^2}}, \quad W_0(s) = s.$$

Because $W_0(s) = s$, we can use the usual ramp filter (3.4.14) without modification. Because $\dot\gamma(s) = (\cos^2\gamma(s))/D_{sd} = W_1^2(s)/D_{sd}$ here, the projection weighting in (3.9.19) becomes

$$\frac{J(s)}{W_1^2} = \frac{1}{D_{sd}} |D_{s0}\cos\gamma(s) - r_{\text{off}}\sin\gamma(s)| \approx \frac{D_{s0}}{\sqrt{D_{sd}^2 + s^2}}, \qquad \text{e,tomo,fan,J˙w1w1,ed} \atop (3.9.25)$$

and the backprojection weighting in (3.9.20) is

$$\frac{1}{W_2^2\, L^2(x,y,\beta)} = \frac{D_{sd}^2}{[\cos\gamma'(x,y,\beta)\, L(x,y,\beta)]^2} = \frac{D_{sd}^2}{[D_{s0} - y_\beta]^2}. \qquad \text{e,tomo,fan,wtb,ed} \atop (3.9.26)$$

Note that as $D_{s0} \to \infty$, the projection and backprojection weightings again approach unity.

IRT *See* `fbp_fan_flat.m`.

The preceding derivation started with the parallel-ray FBP formula. Other formulations are possible, *e.g.*, [117].

3.9.3 FBP for short scans (s,tomo,fan,short)

The preceding analyses have assumed a full 360° rotation. For a 360° rotation, every ray is sampled exactly twice, leading to the 1/2 factor in (3.9.12). There are also fan-beam reconstruction methods that use a *short scan* with less than a full rotation. A standard *short scan* uses $\beta_{\max} = \pi + 2\gamma_{\max}$, so that every point in the equivalent parallel-beam sinogram is sampled at least once. As illustrated in Fig. 3.9.3, some areas of the sinogram are sampled twice, so these methods require appropriate weighting, sometimes called *Parker weighting* [118]. In particular, by the symmetry property (3.9.10), fan-beam sinogram data where $0 < \beta < 2(\gamma_{\max} - \gamma(s))$ correspond to the same rays as $\pi - 2\gamma(s) < \beta < \pi + 2\gamma_{\max}$.

One can compensate for this sampling by applying an additional weighting $w(s, \beta)$ to the ramp-filtered fan-beam sinogram $\check{p}(s, \beta)$ prior to backprojection, such as the following weighting:

$$w(s, \beta) = \begin{cases} q\left(\frac{\beta}{2(\gamma_{\max} - \gamma)}\right), & 0 \leq \beta \leq 2(\gamma_{\max} - \gamma) \\ 1, & 2(\gamma_{\max} - \gamma) < \beta < \pi - 2\gamma \\ q\left(\frac{\pi + 2\gamma_{\max} - \beta}{2(\gamma_{\max} + \gamma)}\right), & \pi - 2\gamma \leq \beta \leq \pi + 2\gamma_{\max}, \end{cases} \qquad \text{e,tomo,fan,short,wsb} \tag{3.9.27}$$

where $q(x) = \sin^2\left(\frac{\pi}{2}x\right)$ and $\gamma = \gamma(s)$. Note that [118, eqn. (12)] has a typo.

IRT *See* `fbp_fan_short_wt.m`.
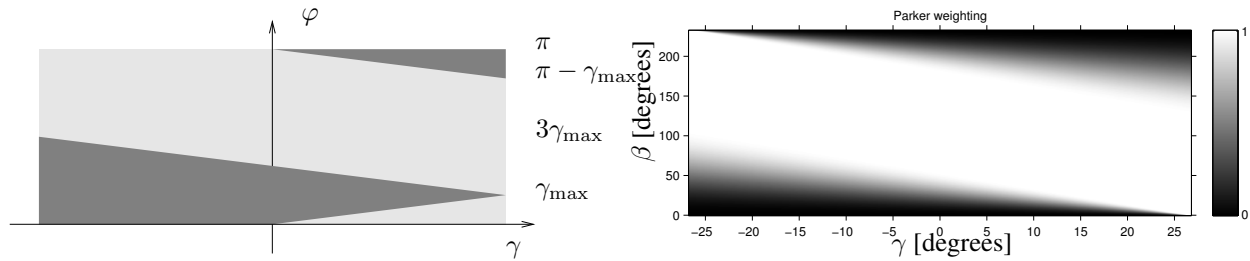

Figure 3.9.3: For short scan with $\beta_{\max} = \pi + 2\gamma_{\max}$, the left figure above illustrates (by darker shading) the areas of a sinogram (in ϕ, γ space) that are sampled twice. The other areas are sampled once. The right figure shows the fan-beam sinogram Parker weighting (3.9.27).

Amazingly, one can also reconstruct an image from less than a short scan [119]. Of course one can apply iterative reconstruction methods to arbitrary geometries. The relative performance of iterative methods and analytical methods for the "less than a short scan" cases is an interesting *open problem*.

s,tomo,fan,bpf

3.9.4 The backproject-filter (BPF) approach (s,tomo,fan,bpf)

Although the filter-backproject approach is used most widely for fan-beam reconstruction, it is also possible to use *backproject-filter* (BPF) methods for fan-beam tomography [13].

Given fan-beam projections $p(s, \beta)$ as defined in (3.9.7), for $\beta \in [0, \beta_{\max}]$, and given a weighting function $w(s, \beta)$, the weighted backprojection is given by

$$b(x, y) = \int_{-s_{\max}}^{s_{\max}} \int_0^{\beta_{\max}} \delta(x \cos\varphi(s, \beta) + y \sin\varphi(s, \beta) - r(s)) \, p(s, \beta) \, w(s, \beta) \, \mathrm{d}s \, \mathrm{d}\beta.$$

We now analyze the impulse response of the sequence of linear operations $f(x, y) \to p(s, \beta) \to b(x, y)$, by considering an object $f(x, y)$ that is a Dirac impulse at (x_0, y_0), for which the fan-beam projections are given by $p(s, \beta) = \delta(x_0 \cos\varphi(s, \beta) + y_0 \sin\varphi(s, \beta) - r(s))$. The overall impulse response of the weighted projection/backprojection operation is thus:

$$\begin{aligned} h(x, y; x_0, y_0) \;=\; & \int_0^{\beta_{\max}} \int_{-s_{\max}}^{s_{\max}} \delta(x \cos\varphi(s, \beta) + y \sin\varphi(s, \beta) - r(s)) \\ & \delta(x_0 \cos\varphi(s, \beta) + y_0 \sin\varphi(s, \beta) - r(s)) \, w(s, \beta) \, \mathrm{d}s \, \mathrm{d}\beta. \end{aligned}$$

Now make the change of variables defined in (3.9.5). the Jacobian determinant of which is given in (3.9.14). Assume that the weighting term $w(s, \beta)$ consists of two terms:
- a term that compensates for the Jacobian determinant in (3.9.14) [13],
- a term that ensures that for any (r, φ) pair that gets contributions from more than one (s, β) pair, these (s, β) pairs are appropriately weighted [5, p. 98] [120]. (No such weighting is needed for a full rotation where $\beta_{\max} = 2\pi$.)

Assume furthermore that $\beta_{\max} \geq \pi + 2\gamma_{\max}$, so that there is complete sampling. Then after making the above change of variables, the impulse response expression simplifies to

$$
\begin{aligned}
h(x, y; x_0, y_0) &= \int_0^\pi \int_{-r_{\max}}^{r_{\max}} \delta(x \cos\varphi + y \sin\varphi - r)\, \delta(x_0 \cos\varphi + y_0 \sin\varphi - r)\, \mathrm{d}r\, \mathrm{d}\varphi \\
&= \int_0^\pi \delta((x - x_0)\cos\varphi + (y - y_0)\sin\varphi)\ 1_{\{|x_0 \cos\varphi + y_0 \sin\varphi| \leq r_{\max}\}}\, \mathrm{d}\varphi \\
&= \int_0^\pi \delta(r_\pm(x - x_0, y - y_0)\cos(\varphi - \angle_\pi(x - x_0, y - y_0)))\ 1_{\{|x_0 \cos\varphi + y_0 \sin\varphi| \leq r_{\max}\}}\, \mathrm{d}\varphi \\
&= \left. \frac{1}{|r_\pm(x - x_0, y - y_0)|}\ 1_{\{|x_0 \cos\varphi + y_0 \sin\varphi| \leq r_{\max}\}} \right|_{\varphi = \angle_\pi(x - x_0, y - y_0) \pm \pi/2},
\end{aligned}
$$

where $r_{\max}$ was defined in (3.9.6). Thus, *within the field of view*, the composition of projection with *appropriately weighted* backprojection is linear and shift invariant, and similarly to Theorem 3.3.1, in polar coordinates the impulse response is [121]: $h(r) = \frac{1}{|r|}$. Using this "restricted" shift invariance, one can formulate an approximate BPF reconstruction method [13]. However, the practical problems described in §3.4.2 are exacerbated here by the inherently finite field of view of the fan-beam geometry.

### 3.9.5 Cone-beam reconstruction (s,3d,cone)

A particularly challenging problem for analytical reconstruction methods is that of reconstructing a 3D object from cone-beam projection views. As X-ray detectors have evolved from 1D to 2D arrays, the practical importance of this problem has increased. The literature on this problem is extensive, and includes both exact and approximate methods, for various types of X-ray source trajectories and detector configurations.

For the case of a circular X-ray source trajectory, the most popular method is the *Feldkamp cone-beam algorithm* or *FDK approach* [122]. This approach extends the fan-beam reconstruction formula to the cone-beam case and matches the fan-beam formula in the plane of the circular source trajectory, but is inexact (due to missing data) away from that plane.

Recently, Katsevich [123] developed a "theoretically exact" FBP type of reconstruction method for cone-beam reconstruction from a *helical* source trajectory, a significant breakthrough in that field. As a result, this topic is evolving rapidly, *e.g.*, [124]. Versions of the *Fourier-slice theorem* have even been proposed for fan-beam and cone-beam geometries [125]. In practice, usually "approximate" algorithms are often used rather than the exact methods to save computation. A typical approximate algorithm involves some rebinning, ramp filtering, and weighted backprojection steps, *e.g.*, [126]. Here, we summarize only the classical FDK method for a circular trajectory.

The basic idea of the FDK method is to filter the data measured along each row of the detector as if it were part of a 2D fan-beam acquisition, and then to perform 3D backprojection. With this approximation, the central slice is reconstructed exactly as it would be by conventional 2D fan-beam methods, whereas the non-central slices have artifacts that increase with distance from the central slice.

3.9.5.1 Equidistant case (flat detector)
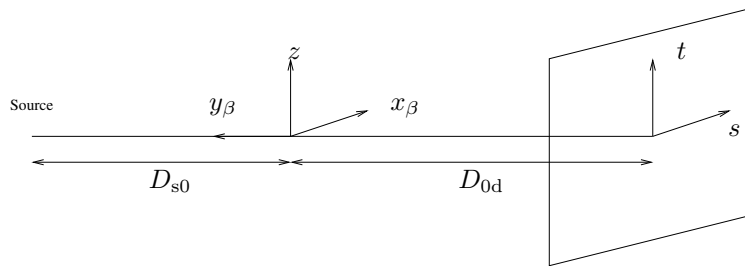
fig˙tomo˙cone

Figure 3.9.4: Cone-beam flat-detector geometry.

Fig. 3.9.4 illustrates the flat-detector cone-beam geometry, where the rotated coordinates (x_β, y_β) were defined in (3.9.16). As in Fig. 3.9.1 we let β denote the angle of the source point counter-clockwise from the y axis. The cone-beam projections are given by

$$p(s, t; \beta) = \int_{\mathcal{L}(s,t,\beta)} f(x, y, z) \, d\ell,$$

where

$$\vec{p}_0 = (-D_{s0} \sin\beta, D_{s0} \cos\beta, 0) \tag{3.9.28}$$

$$\vec{p}_1 = (s \cos\beta + D_{0d} \sin\beta, s \sin\beta - D_{0d} \cos\beta, t) \tag{3.9.29}$$

$$\mathcal{L}(s, t, \beta) = \left\{ \vec{p}_0 + \alpha \frac{\vec{p}_1 - \vec{p}_0}{\|\vec{p}_1 - \vec{p}_0\|} : \alpha \in \mathbb{R} \right\}. \tag{3.9.30}$$

<div style="text-align:right">e,3d,cone,Lstb</div>

Note that $\vec{p}_1 - \vec{p}_0 = (s \cos\beta + D_{sd} \sin\beta, s \sin\beta - D_{sd} \cos\beta, t)$ and $\|\vec{p}_1 - \vec{p}_0\| = \sqrt{D_{sd}^2 + s^2 + t^2}$.

Consider one row of the measured projection at angle β and vertical position t. That row forms a *tilted fan* with the source point, with modified distances

$$D'_{s0} = D_{s0} \sqrt{1 + (t/D_{sd})^2}$$

$$D'_{sd} = D_{sd} \sqrt{1 + (t/D_{sd})^2}.$$

Following §3.9.2.2 we apply the projection weighting given in (3.9.25) but with D_{s0} and D_{sd} replaced by D'_{s0} and D'_{sd} respectively, *i.e.*,

$$\frac{D'_{s0}}{\sqrt{(D'_{sd})^2 + s^2}} = \frac{D_{s0} \sqrt{1 + (t/D_{sd})^2}}{\sqrt{D_{sd}^2 + s^2 + t^2}}. \tag{3.9.31}$$

<div style="text-align:right">e,3d,cone,wtp</div>

Then, we apply the usual ramp filter (3.4.14) to the measurements from each row of the detector. Then we perform 3D cone-beam backprojection using the image-domain weighting given in (3.9.26). No modifications of (3.9.26) are needed because all quantities therein are "magnified" by the same factor $\sqrt{1 + (t/D_{sd})^2}$ when considering the tilted fan, so the scaling factor cancels out. To summarize, the FDK algorithm consists of the following steps.

- Step 1. Compute weighted projections

$$\tilde{p}(s, t; \beta) = w_1(s, t) \, p(s, t; \beta), \qquad w_1(s, t) = \frac{D_{s0} \sqrt{1 + (t/D_{sd})^2}}{\sqrt{D_{sd}^2 + s^2 + t^2}}. \tag{3.9.32}$$

<div style="text-align:right">e,3d,cone,pst,w1</div>

- Step 2. Filter each row of those projections using the ordinary ramp filter:

$$\check{p}(s, t; \beta) = \tilde{p}(s, t; \beta) * h(s), \tag{3.9.33}$$

<div style="text-align:right">e,3d,cone,pst,filter</div>

where $h(s)$ denotes the ramp filter given in (3.4.13) or (3.4.14).

- Step 3. Perform weighted cone-beam backprojection of those filtered projections:

$$\hat{f}(x, y, z) = \frac{1}{2} \int_0^{2\pi} w_2(x, y, \beta) \, \check{p}\left(\frac{D_{sd}}{D_{s0} - y_\beta} x_\beta, \frac{D_{sd}}{D_{s0} - y_\beta} z; \beta \right) d\beta, \qquad w_2(x, y, \beta) = \frac{D_{sd}^2}{(D_{s0} - y_\beta)^2}. \tag{3.9.34}$$

<div style="text-align:right">e,3d,cone,back</div>

(The factor $\frac{D_{sd}}{D_{s0} - y_\beta}$ is a magnification factor.)

3.9.5.2　Equiangular case (3rd generation multi-slice CT)

For a 3rd-generation multi-slice CT scanner, the FDK algorithm has the same basic steps as above, except that the 1D weighting in (3.9.32) is replaced by:

$$w_1(s, t) = \frac{D'_{s0}}{D'_{sd}} \cos\frac{s}{D'_{sd}} = \frac{D_{s0}}{D_{sd}} \cos\frac{s}{D_{sd} \sqrt{1 + (t/D_{sd})^2}}, \tag{3.9.35}$$

<div style="text-align:right">e,3d,cone,pst,w1,arc</div>

the filtering in (3.9.33) uses the modified ramp filter (3.9.21) or (3.9.24), and the 2D weighting in (3.9.34) is replaced by (3.9.23).

s,tomo,summ ## 3.10   **Summary** (s,tomo,summ)

This chapter has reviewed analytical methods for tomographic image reconstruction. We have considered the parallel-beam geometry, fan-beam geometries for both flat and curved detectors, and the cone-beam geometry with a flat detector. For analytical methods, each geometry requires its own derivation. In contrast, for iterative image reconstruction, the basic formulations are the same for any geometry.

Interestingly, even though the topics in this chapter have been studied for decades, advances continue to be made. For example, recently the subject of reconstructing regions of interest (from truncated sinogram data) has had breakthroughs [58, 127–129]. And there is ongoing progress on image reconstruction from the exponential Radon transform [130–132].

Because of the shift invariance of (parallel-beam) projection and backprojection, the primary tool for understanding these methods is Fourier analysis. It is something of a leap from the Fourier focus of this chapter to the linear algebra focus of subsequent chapters; the next chapter attempts to partly bridge these approaches by using operators, the continuous-space analog of matrices.

s,tomo,prob ## 3.11   **Problems** (s,tomo,prob)

p,tomo,ex,1-r2 **Problem 3.1** *Determine the Radon transform of the 2D function [133]* $f_\circ(r) = \left(1 - r^2\right) \operatorname{rect}(r/2)$.

p,tomo,ex,sqrt **Problem 3.2** *Determine the Radon transform of the 2D function* $f_\circ(r) = 2\sqrt{1 - r^2}\ 1_{\{|r| \leq 1\}}$.

p,tomo,separable **Problem 3.3** *Use the Fourier-slice theorem to show that the Radon transform of any separable function* $f(x, y) = a(x)\, b(y)$ *is given by*

$$p_\varphi(r) = \frac{1}{|\cos\varphi|}\, a\left(\frac{r}{\cos\varphi}\right) * \frac{1}{|\sin\varphi|}\, b\left(\frac{r}{\sin\varphi}\right).$$

Problem 3.4 *Show that the Radon transform of the function* $f(x, y) = \operatorname{sinc}(x)\operatorname{sinc}(y)$ *is given by*

$$p_\varphi(r) = \frac{1}{\max(|\cos\varphi|, |\sin\varphi|)}\, \operatorname{sinc}\left(\frac{r}{\max(|\cos\varphi|, |\sin\varphi|)}\right).$$

p,tomo,star **Problem 3.5** *Consider the following "star function" [12]:*

$$\operatorname{star}(r, \varphi) \triangleq \frac{1}{|r|} \sum_{n=1}^{N} \delta((\varphi - \varphi_n) \bmod \pi).$$

Show that the 2D FT of this function is $\operatorname{star}(\rho, \Phi \pm \pi/2)$.

Problem 3.6 *Prove each of the Radon transform properties in §3.2.3.*

Problem 3.7 *Find a Radon transform property for an* affine transformation *of the object* $f(x, y)$, i.e.,

$$f(a_{11}x + a_{12}y + b_1, a_{21}x + a_{22}y + b_2)$$

with $a_{11}a_{22} - a_{12}a_{21} \neq 0$.

Problem 3.8 *Show that if* $0 < a \leq b$ *then*

$$\frac{1}{a} \operatorname{rect}\left(\frac{x}{a}\right) * \frac{1}{b} \operatorname{rect}\left(\frac{x}{b}\right) = \frac{b+a}{2ba} \operatorname{tri}\left(\frac{2x}{b+a}\right) - \frac{b-a}{2ba} \operatorname{tri}\left(\frac{2x}{b-a}\right),$$

where tri *was defined in (3.2.12).*

Problem 3.9 *Derive the projections of a square as given in (3.2.11).*   *(Need typed.)*

p,radon,flat **Problem 3.10** *Find a nonzero object $f(x, y)$ (other than a Dirac impulse) whose projections have the property that they depend only on φ over their support, i.e.,*

$$p_\varphi(r) = \begin{cases} g_\varphi, & r_{\min}(\varphi) \leq r \leq r_{\max}(\varphi) \\ 0, & \text{otherwise,} \end{cases}$$

for some functions g_φ, $r_{\min}(\varphi)$, and $r_{\max}(\varphi)$ that depend on $f(x, y)$.

Generalize to the case of fan-beam projections, i.e., find the object $f(x, y)$ for which $p(s, \beta) = \text{rect}\left(\frac{s}{2s_0}\right)$, where $s_0 \leq s_{\max}$. (Assume $r_{\text{off}} = 0$ for simplicity.)

Problem 3.11 *Let $p_\varphi(r)$ denote the Radon transform of a disk object as considered in Example 3.2.1. Determine (analytically) $\check{p}_\varphi(r)$, the corresponding ramp-filtered projections, and plot.* *(Need typed.)*

p,tomo,spline **Problem 3.12** *Given noisy, blurred, samples of the Radon transform of an object, one interesting reconstruction approach is to first fit 1D spline functions to each projection view, and then filter those continuous-space fitted projections using* analytical *expressions, and then backproject [134]. In other words, we make the approximation $p_\varphi(r) = \sum_{n=-\infty}^{\infty} c_n b(r/\Delta_{\text{R}} - n)$, where the coefficients c_n are determined from the sampled projections by filtering [135]. The ramp-filtered projections $\check{p}_\varphi(r)$ have the form $\check{p}_\varphi(r) = \sum_{n=-\infty}^{\infty} c_n \check{b}(r/\Delta_{\text{R}} - n)$. Find an analytical expression for $\check{b}(\cdot)$ when $b(\cdot)$ is a cubic B-spline.*

p,tomo,freq,dis **Problem 3.13** *An interesting property of the Radon transform is the* frequency-distance relation *or* frequency-distance principle *that describes the characteristics of the 2D Fourier transform of a sinogram [97, 98, 136, 137].*
- *Consider $f(x, y) = \delta(x - x_0, y - y_0)$ and take the 2D FT of its sinogram to see where it is nonzero.*
- *Analyze the impulse response in the sinogram domain of such an apodization.*
- *Analyze how much noise reduction could be achieved with such method.*
- *Take the 2D sinogram of an image (over 360° for simplicity), compute its 2D DFT, and set to zero the coefficients outside the* bowtie region *described in the papers cited above, then inverse transform and reconstruct the image by FBP. Observe the effects.*

Problem 3.14 *§3.3 is missing an example where the laminogram $f_{\text{b}}(x, y)$ can be found analytically. Find an object $f(x, y)$ whose projections ($p_\varphi(r)$ or $P_\varphi(\nu)$) and laminogram $f_{\text{b}}(x, y)$ have simple analytical expressions. Hint: [11, p. 338] may be useful.*

tomo,back,general **Problem 3.15** *Prove the general back-projection relationship (3.15).*

Problem 3.16 *§3.4.6 described how it is preferable to sample the (band-limited) ramp filter in the space domain for the FBP method. For the BPF method, would it be advantageous to find the impulse response $h(r)$ of the (band-limited) cone filter and then sample it instead of sampling the cone directly? Discuss.*

Problem 3.17 *Some tomographic imaging systems cannot measure the projection views at every projection angle. Such angularly incomplete data is known as* limited angle *tomography and is notoriously challenging.*
One way to model the effects of such missing projection views is to set $w(\varphi)$ to zero in the backprojection formula (3.3.1) for angles φ that are missing, and to unity otherwise. Suppose we apply this idea to a system that only records projection views where $\varphi \in [0, 7\pi/8]$.
Sketch the support of the spectrum of the laminogram, i.e., $F_{\text{b}}(u, v)$ in this case.
Explain why this is called the "missing wedge" problem (in 2D) or the "missing cone" in such 3D problems.
*Explain why the BPF method cannot work in this case.* *(Need typed.)*

Problem 3.18 *Let $b_\varphi(x, y) = p_\varphi(x \cos\varphi + y \sin\varphi)$ denote the image formed by backprojection of a projection at angle φ, and let $B_\varphi(u, v)$ denote its 2D Fourier transform. Relate $B_\varphi(u, v)$ to $F(u, v)$.*
Hint: relate $B_0(u, v)$ to $F(u, 0) \delta(v)$. *(Need typed.)*

Problem 3.19 *The set (3.9.4) is too large to be realistic for a practical system like that illustrated in Fig. 3.9.1. Find a more realistic expression for $\mathcal{L}(s, \beta)$.*

p,tomo,artifact **Problem 3.20** *Each of the images in Fig. 3.11.1 exhibits some type of artifact due to data limitations or errors. Match the figure with the corresponding problem in the following list.*

1. *Limited projection angular range (less than* $180°$*).*
2. *Under-sampled projection view angles.*
3. *Single detector channel with miscalibrated gain.*
4. *Misaligned detector (radial shift).*
5. *Projection views over* $[0, 180°]$ *instead of* $[0, 180° \frac{n_A - 1}{n_A}]$
6. *Fan-beam data into parallel-beam reconstructor*

a   b   c

d   e   f
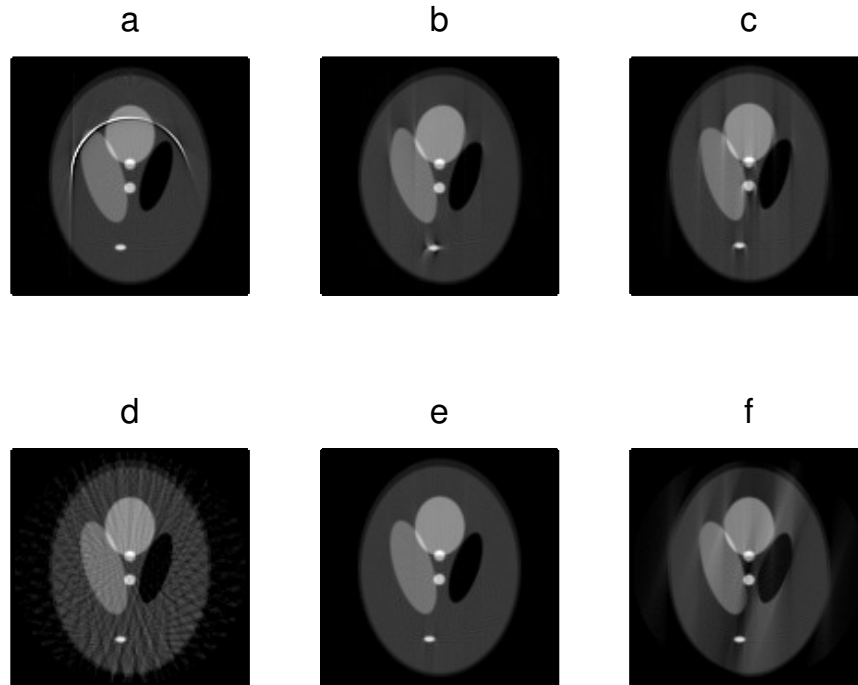
fig˙tomo˙artifact

Figure 3.11.1: Illustration of common artifacts for Problem 3.20.

Problem 3.21 *Modify (3.3.2) and (3.3.5) to consider the case of a* $360°$ *rotation. Show that the impulse response is given by* $h(r, \varphi) = \frac{1}{|r|} [w(\varphi + \pi/2) + w(\varphi + 3\pi/2)]$ *for* $\varphi \in [-\pi/2, \pi/2]$ *and the frequency response is* $H(\rho, \Phi) = \frac{1}{|\rho|} [w(\Phi) + w(\Phi + \pi)]$. *These relations are useful for analyzing* $360°$ *SPECT scans.*   *(Need typed.)*

Problem 3.22 *Find a relationship between* $\check{P}_\varphi(\nu)$ *and* $F_b(u, v)$ *or* $F_b(\rho, \Phi)$ *to complete the bottom link in Fig. 3.3.3.*

p,tomo,fbp,rect   **Problem 3.23** *Find* $\check{P}_\varphi(\nu)$ *and* $\check{p}_\varphi(r)$ *in Example 3.4.5 when* $\varphi = 0$.

,tomo,ramp,gauss   **Problem 3.24** *Suppose the ideal ramp filter is applied to the projections* $p_\varphi(r)$ *of a* gaussian *object* $f(x, y) = w^{-2} e^{-\pi(r/w)^2}$. *Determine analytically the resulting filtered projections* $\check{p}_\varphi(r)$ *and plot.*

,ramp,apod,gauss   **Problem 3.25** *Suppose the ideal ramp filter* $|\nu|$ *is apodized by a gaussian* $A(\nu) = e^{-\pi\nu^2}$ *instead of by the discontinuous rect function (3.4.12). Determine the resulting impulse response* $h_a(r)$ *of the apodized ramp filter.*

o,ramp,apod,hann   **Problem 3.26** *Suppose that a* Hanning window *is applied to the ramp filter,* i.e.,

$$A(\nu) = \text{rect}\left(\frac{\nu}{2\nu_0}\right) \frac{1 + \cos(\pi\nu/\nu_0)}{2}$$

in (3.4.10). Using Fourier transform properties, find analytically *the impulse response* $h_a(r)$ *of the apodized ramp filter, and plot it. Compare to Fig. 3.4.6 and comment on the advantages and disadvantages of this choice.*

tomo,ramp,apod,tri **Problem 3.27** *Suppose the ramp filter is apodized using a triangular window function* $A(\nu) = \mathrm{tri}(\nu/\nu_c)$. *Find an analytical expression for the impulse response* $h_\mathrm{a}(r)$ *of the resulting apodized ramp filter using symbolic integration.*

tomo,fbp,apod,exp **Problem 3.28** *Suppose the apodizer* $A(\nu) = \mathrm{e}^{-a|\nu|}$ *is used in the FBP method. Find the resulting image PSF* $h(r)$.

Problem 3.29 *Real tomographs can be aligned imprecisely, leading to offset projections:* $q_\varphi(r) = p_\varphi(r - \tau)$ *for* some *offset center of rotation* τ. *Determine the PSF of such an imaging system when the FBP method is applied to* $q_\varphi(r)$. *(Solve?)*

Problem 3.30 *Would the* inverse filter *approach of §3.5.4 work if we used nearest-neighbor interpolation, i.e.,* $h(r) = \mathrm{rect}(r/\Delta_\mathrm{R})$? *Explain why or why not.*

Problem 3.31 *A PET scanner measures line integrals along chords connecting detector pairs typically arranged around a circle. The natural measurement model would be* $g(\varphi_1, \varphi_2) = \int_{\mathcal{L}(\varphi_1, \varphi_2)} f(x, y) \, \mathrm{d}\ell$, *where* $\mathcal{L}(\varphi_1, \varphi_2)$ *denotes the set of points along the chord connecting the point* (r_0, φ_1) *with the point* (r_0, φ_2) *(in polar coordinates), where* r_0 *is the radius of the system. Following §3.9, derive a BPF method for this geometry. It may be easier to use the transformed parameterization:* $\varphi = (\varphi_1 + \varphi_2)/2$, $\gamma = (\varphi_2 - \varphi_1)/2$..

Problem 3.32 *Using (3.2.10) and (3.2.20), determine the Radon transform of an ellipse object centered at* (c_x, c_y) *with major axes of half lengths* r_x, r_y, *tilted at an angle* χ *with respect to the horizontal axis. Assume the function is unity within the ellipse and zero outside. Generalize to the case of fan-beam projections.*

p,tomo,lambda **Problem 3.33** *The method called* lambda tomography *is a* local tomography *approach where one back-projects the second derivative* $\frac{\partial^2}{\partial r^2} p_\varphi(r)$ *of the projections [138–141]. Show that the frequency-domain relationship between the resulting backprojected image and the original image is*

$$B(u, v) = -2\pi \Lambda(\rho) \, F(u, v),$$

where $\Lambda(\rho) = 2\pi |\rho|$ *is the square root of* $-\Delta$, *the* positive Laplace operator. *In 2D, the positive Laplace operator is* $-\Delta = \frac{\mathrm{d}^2}{\mathrm{d}x^2} + \frac{\mathrm{d}^2}{\mathrm{d}y^2}$, *cf. (2.4.1), which has Fourier transform* $\hat{\Delta}(\rho) = (2\pi\rho)^2$.

p,tomo,hilbert **Problem 3.34** *A disadvantage of the ramp filter in (3.4.2) and the Hilbert transform in (3.4.6) is that they both depend on* $p_\varphi(r)$ *for all* $r \in \mathbb{R}$. *Therefore, if the projection data are* truncated, *meaning available only for* r *in a finite interval* $[r_\mathrm{min}, r_\mathrm{max}]$, *then FBP methods based on the ramp filter will produce very large artifacts.*
Following [127], consider what happens if we simply differentiate each projection and then back project:

$$b(x, y) \triangleq \frac{-1}{2\pi} \int_0^\pi \frac{\mathrm{d}}{\mathrm{d}r} p_\varphi(r) \bigg|_{r = x\cos\varphi + y\sin\varphi} \mathrm{d}\varphi.$$

<div align="right">e,tomo,back,deriv
(3.11.1)</div>

- *Using (3.3.8) show that*

$$B(u, v) = -\imath \, \mathrm{sgn}(v) \, F(u, v).$$

  In other words, for each x, $b(x, y)$ *is the* Hilbert *transform of* $f(x, y)$ *along the* y-*direction.*
- *Determine* $b(x, y)$ *analytically for the case* $f(x, y) = \circ r/r_0$. *Hint: use Example 3.4.4, and see Fig. 3.11.2.*
- *Sample the solution in the previous part (ala Fig. 3.11.2) and apply a FFT-based inverse Hilbert transform method to recover* $f[n, m]$ *(approximately) from* $b[n, m]$. *Hint: use mirror end conditions along the* y *direction to avoid artifacts due to discontinuities at the image edge.*
- *todo: try it in matlab*
  todo: compare the FFT-based inverse Hilbert transform approach to the finite Hilbert inverse *described in [142] [127] [143].*

Bibliography

slepian:83:sco [1] D. Slepian. Some comments on Fourier analysis, uncertainty and modeling. *SIAM Review*, 25(3):379–93, July 1983.

helgason:80 [2] S. Helgason. *The Radon transform.* Birkhauser, 1980. Progress in Mathematics V.

b(x,y)
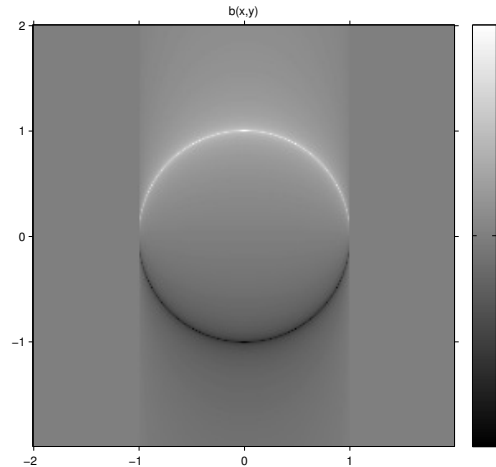
fig˙tomo˙prob˙hilbert˙disk

Figure 3.11.2: Backprojection of derivative of each projection of a disk of radius $r_0 = 1$, for Problem 3.34.

deans:83	[3]	S. R. Deans. *The Radon transform and some of its applications*. Wiley, New York, 1983. 1993 2nd edition by Krieger Publishing Co., Malabar, Florida.
natterer:86	[4]	F. Natterer. *The mathematics of computerized tomography*. Teubner-Wiley, Stuttgart, 1986.
kak:88	[5]	A. C. Kak and M. Slaney. *Principles of computerized tomographic imaging*. IEEE Press, New York, 1988.
natterer:01	[6]	F. Natterer and F. Wübbeling. *Mathematical methods in image reconstruction*. Soc. Indust. Appl. Math., Philadelphia, 2001.
edholm:87:lii	[7]	P. R. Edholm and G. T. Herman. Linograms in image reconstruction from projections. *IEEE Trans. Med. Imag.*, 6(4):301–7, December 1987.
marzetta:99:asr	[8]	T. L. Marzetta and L. A. Shepp. A surprising Radon transform result and its application to motion detection. *IEEE Trans. Im. Proc.*, 8(8):1039–49, August 1999.
zhang:02:ttf	[9]	F. Zhang, G. Bi, and Y. Q. Chen. Tomography time-frequency transform. *IEEE Trans. Sig. Proc.*, 50(6):1289–97, June 2002.
bracewell:56:sii	[10]	R. N. Bracewell. Strip integration in radio astronomy. *Aust. J. Phys.*, 9:198–217, 1956.
bracewell:00	[11]	R. Bracewell. *The Fourier transform and its applications*. McGraw-Hill, New York, 3 edition, 2000.
smith:73:irf	[12]	P. R. Smith, T. M. Peters, and R. H. T. Bates. Image reconstruction from finite numbers of projections. *J. Phys. A: Math. Nucl. Gen.*, 6(3):361–82, March 1973.
gullberg:95:bff	[13]	G. T. Gullberg and G. L. Zeng. Backprojection filtering for variable orbit fan-beam tomography. *IEEE Trans. Nuc. Sci.*, 42(4-1):1257–66, August 1995.
derosier:68:rot	[14]	D. De Rosier and A. Klug. Reconstruction of three-dimensional structures from electron micrographs. *Nature*, 217(5124):130–8, January 1968.
herman:72:tdm	[15]	G. T. Herman. Two direct methods for reconstructing pictures from their projections: a comparative study. *Comp. Graphics and Im. Proc.*, 1(2):123–44, August 1972.
sweeney:73:rot	[16]	D. W. Sweeney and C. M. Vest. Reconstruction of three-dimensional refractive index fields from multidirectional interferometric data. *Appl. Optics*, 12(11):2649–, November 1973.
mersereau:74:dro	[17]	R. M. Mersereau and A. V. Oppenheim. Digital reconstruction of multidimensional signals from their projections. *Proc. IEEE*, 62(10):1319–38, October 1974.
mersereau:74:rms	[18]	R. M. Mersereau. Recovering multidimensional signals from their projections. *Comp. Graphics and Im. Proc.*, 1(2):179–85, October 1974.
mersereau:76:dft	[19]	R. M. Mersereau. Direct Fourier transform techniques in 3-D image reconstruction. *Computers in Biology and Medicine*, 6(4):247–58, October 1976.
stark:81:aio	[20]	H. Stark, J. W. Woods, I. Paul, and R. Hingorani. An investigation of computerized tomography by direct Fourier inversion and optimimum interpolation. *IEEE Trans. Biomed. Engin.*, 28(7):496–505, July 1981.
stark:81:dfr	[21]	H. Stark, J. W. Woods, I. Paul, and R. Hingorani. Direct Fourier reconstruction in computer tomography. *IEEE Trans. Acoust. Sp. Sig. Proc.*, 29(2):237–44, April 1981.
lewitt:83:rat	[22]	R. M. Lewitt. Reconstruction algorithms: transform methods. *Proc. IEEE*, 71(3):390–408, March 1983.
natterer:85:fri	[23]	F. Natterer. Fourier reconstruction in tomography. *Numerische Mathematik*, 47(3):343–53, September 1985.

osullivan:85:afs [24] J. D. O'Sullivan. A fast sinc function gridding algorithm for Fourier inversion in comuter tomography. *IEEE Trans. Med. Imag.*, 4(4):200–7, December 1985.

matej:90:ahs [25] S. Matej and I. Bajla. A high-speed reconstruction from projections using direct Fourier method with optimized parameters-an experimental analysis. *IEEE Trans. Med. Imag.*, 9(4):421–9, December 1990.

cheung:91:mfr [26] W. K. Cheung and R. M. Lewitt. Modified Fourier reconstruction method using shifted transform samples. *Phys. Med. Biol.*, 36(2):269–77, February 1991.

tabei:92:bbu [27] M. Tabei and M. Ueda. Backprojection by upsampled Fourier series expansion and interpolated FFT. *IEEE Trans. Im. Proc.*, 1(1):77–87, January 1992.

alliney:93:otp [28] S. Alliney, S. Matej, and I. Bajla. On the possibility of direct Fourier reconstruction from divergent-beam projections. *IEEE Trans. Med. Imag.*, 12(2):173–81, June 1993.

schomberg:95:tgm [29] H. Schomberg and J. Timmer. The gridding method for image reconstruction by Fourier transformation. *IEEE Trans. Med. Imag.*, 14(3):596–607, September 1995.

dusaussoy:96:vav [30] N. J. Dusaussoy. VOIR: a volumetric image reconstruction algorithm based on Fourier techniques for inversion of the 3-D Radon transform. *IEEE Trans. Im. Proc.*, 5(1):121–31, January 1996.

bellon:97:fdf [31] P. L. Bellon and S. Lanzavecchia. Fast direct Fourier methods, based on one- and two-pass coordinate transformations, yield accurate reconstructions of x-ray CT clinical images. *Phys. Med. Biol.*, 42(3):443–64, March 1997.

lanzavecchia:97:tmw [32] S. Lanzavecchia and P. L. Bellon. The moving window Shannon reconstruction in direct and Fourier domain: application in tomography. *Scanning Microscopy Intl.*, 11:155–70, 1997.

choi:98:dfr [33] H. Choi and D. C. Munson. Direct-Fourier reconstruction in tomography and synthetic aperture radar. *Intl. J. Imaging Sys. and Tech.*, 9(1):1–13, 1998.

seger:98:tdr [34] M. M. Seger. Three-dimensional reconstruction from cone-beam data using an efficient Fourier technique combined with a special interpolation filter. *Phys. Med. Biol.*, 43(4):951–60, April 1998.

gottlieb:00:otd [35] D. Gottlieb, B. Gustafsson, and P. Forssen. On the direct Fourier method for computer tomography. *IEEE Trans. Med. Imag.*, 19(3):223–32, March 2000.

walden:00:aot [36] J. Waldén. Analysis of the direct Fourier method for computer tomography. *IEEE Trans. Med. Imag.*, 19(3):211–22, March 2000.

potts:01:anl [37] D. Potts and G. Steidl. A new linogram algorithm for computerized tomography. *IMA J. Numer. Anal.*, 21(3):769–82, July 2001.

fourmont:03:nef [38] K. Fourmont. Non-equispaced fast Fourier transforms with applications to tomography. *J. Fourier Anal. and Appl.*, 9(5):431–50, September 2003.

penczek:04:gbd [39] P. A. Penczek, R. Renka, and H. Schomberg. Gridding-based direct Fourier inversion of the three-dimensional ray transform. *J. Opt. Soc. Am. A*, 21(4):499–509, April 2004.

matej:04:iti [40] S. Matej, J. A. Fessler, and I. G. Kazantsev. Iterative tomographic image reconstruction using Fourier-based forward and back- projectors. *IEEE Trans. Med. Imag.*, 23(4):401–12, April 2004.

higgins:88:aht [41] W. E. Higgins and D. C. Munson. A Hankel transform approach to tomographic image reconstruction. *IEEE Trans. Med. Imag.*, 7(1):59–72, March 1988.

deman::ahs [42] B. De Man and S. Basu. A high-speed, low-artifact approach to projection and backprojection, 2002.

chu:77:tdi [43] G. Chu and K. C. Tam. Three-dimensional imaging in the positron camera using Fourier techniques. *Phys. Med. Biol.*, 22(2):245–65, March 1977.

colsher:80:ftd [44] J. G. Colsher. Fully three dimensional positron emission tomography. *Phys. Med. Biol.*, 25(1):103–15, January 1980.

abramowitz:64 [45] M. Abramowitz and I. A. Stegun. *Handbook of mathematical functions*. Dover, New York, 1964.

barrett:03 [46] H. H. Barrett and K. J. Myers. *Foundations of image science*. Wiley, New York, 2003.

grafakos:04 [47] L. Grafakos. *Classical and modern Fourier analysis*. Pearson, NJ, 2004.

radon:1917:otd [48] J. Radon. On the determination of functions from their integrals along certain manifold. *Berichte Sächs. Akad. Wiss. (Leipzig)*, 69:262–78, 1917. Uber die Bestimmung von Funktionen durch ihre Intergralwerte Langs gewisser Manningfultigkeiten.

radon:86:otd [49] J. Radon. On the determination of functions from their integral values along certain manifolds. *IEEE Trans. Med. Imag.*, 5(4):170–6, December 1986.

servieres:04:slb [50] M. C. J. Servières, N. Normand, P. Subirats, and J. Guédon. Some links between continuous and discrete Radon transform. In *Proc. SPIE 5370, Medical Imaging 2004: Image Proc.*, pages 1961–71, 2004.

ramachandran:71:tdr [51] G. N. Ramachandran and A. V. Lakshminarayanan. Three-dimensional reconstruction from radiographs and electron micrographs: application of convolutions instead of Fourier transforms. *Proc. Natl. Acad. Sci.*,

68(9):2236–40, September 1971.

bracewell:67:iof [52] R. N. Bracewell and A. C. Riddle. Inversion of fan-beam scans in radio astronomy. *The Astrophysical Journal*, 150:427–34, November 1967.

crawford:91:cfa [53] C. R. Crawford. CT filtration aliasing artifacts. *IEEE Trans. Med. Imag.*, 10(1):99–102, March 1991.

macovski:83 [54] A. Macovski. *Medical imaging systems*. Prentice-Hall, New Jersey, 1983.

gelfand:77 [55] I. M. Gelfand and G. E. Shilov. *Generalized functions, Properties and operations*. Academic Press, New York, 1977. Vol. 1.

zeng:04:nnp [56] G. L. Zeng. Nonuniform noise propagation by using the ramp filter in fan-beam computed tomography. *IEEE Trans. Med. Imag.*, 23(6):690–5, June 2004.

shepp:74:tfr [57] L. A. Shepp and B. F. Logan. The Fourier reconstruction of a head section. *IEEE Trans. Nuc. Sci.*, 21(3):21–43, June 1974.

clackdoyle:04:alc [58] R. Clackdoyle and Frédéric Noo. A large class of inversion formulae for the 2D Radon transform of functions of compact support. *Inverse Prob.*, 20(4):1281–92, August 2004.

horbelt:02:dot [59] S. Horbelt, M. Liebling, and M. Unser. Discretization of the Radon transform and of its inverse by spline convolutions. *IEEE Trans. Med. Imag.*, 21(4):363–76, April 2002.

unser:95:cbi [60] M. Unser, P. Thevenaz, and L. Yaroslavsky. Convolution-based interpolation for fast, high quality rotation of images. *IEEE Trans. Im. Proc.*, 4(10):1371–81, October 1995.

fessler::eop [61] J. A. Fessler. Equivalence of pixel-driven and rotation-based backprojectors for tomographic image reconstruction, 1997. Rejected by IEEE Transactions on Medical Imaging.

fessler:95:rpo [62] J. A. Fessler. Resolution properties of regularized image reconstruction methods. Technical Report 297, Comm. and Sign. Proc. Lab., Dept. of EECS, Univ. of Michigan, Ann Arbor, MI, 48109-2122, August 1995.

horbelt:02:fdf [63] S. Horbelt, M. Liebling, and M. Unser. Filter design for filtered back-projection guided by the interpolation model. In *Proc. SPIE 4684, Medical Imaging 2002: Image Proc.*, pages 806–13, 2002.

duerinckx:78:nls [64] A. J. Duerinckx, L. M. Zatz, and A. Macovski. Non-linear smoothing filters and noise structure in computed tomography (CT) scanning: a preliminary report. In *Proc. SPIE 152, Recent & Future Developments in Medical Im.*, pages 19–25, 1978.

king:83:awf [65] M. A. King, P. W. Doherty, R. B. Schwinger, and B. C. Penney. A Wiener filter for nuclear medicine images. *Med. Phys.*, 10(6):876–80, November 1983.

hutchins:87:cls [66] G. D. Hutchins, W. L. Rogers, N. H. Clinthorne, R. A. Koeppe, and R. D. Hichwa. Constrained least-squares projection filtering: a new method for the reconstruction of emission computed tomographic images. *IEEE Trans. Nuc. Sci.*, 34(1):379–83, February 1987.

penney:88:mcl [67] B. C. Penney, M. A. King, R. B. Schwinger, S. P. Baker, and P. W. Doherty. Modifying constrained least-squares restoration for application to SPECT projection images. *Med. Phys.*, 15(3):334–42, May 1988.

abidi:90:rnf [68] M. A. Abidi and P. B. Davis. Radial noise filtering in positron emission tomography. *Optical Engineering*, 29(5):567–74, May 1990.

hutchins:90:cls [69] G. D. Hutchins, W. L. Rogers, P. Chiao, R. Raylman, and B. W. Murphy. Constrained least-squares projection filtering in high resolution PET and SPECT imaging. *IEEE Trans. Nuc. Sci.*, 37(2):647–51, April 1990.

hebert:91:aif [70] T. J. Hebert and S. S. Gopal. An improved filtered back-projection algorithm using pre-processing. In *Proc. IEEE Nuc. Sci. Symp. Med. Im. Conf.*, volume 3, pages 2068–72, 1991.

sauer:91:nfo [71] K. Sauer and B. Liu. Nonstationary filtering of transmission tomograms in high photon counting noise. *IEEE Trans. Med. Imag.*, 10(3):445–52, September 1991.

hebert:92:auo [72] T. J. Hebert. A union of deterministic and stochastic methods for image reconstruction. In *Proc. IEEE Nuc. Sci. Symp. Med. Im. Conf.*, volume 2, pages 1117–9, 1992.

fessler:93:tru [73] J. A. Fessler. Tomographic reconstruction using information weighted smoothing splines. In H H Barrett and A F Gmitro, editors, *Information Processing in Medical Im.*, volume 687 of *Lecture Notes in Computer Science*, pages 372–86. Springer-Verlag, Berlin, 1993.

hsieh:98:asa [74] J. Hsieh. Adaptive streak artifact reduction in computed tomography resulting from excessive x-ray photon noise. *Med. Phys.*, 25(11):2139–47, November 1998.

lariviere:98:ioa [75] P. J. La Riviere, X. Pan, and B. C. Penney. Ideal-observer analysis of lesion detectability in planar, conventional SPECT, and dedicated SPECT scintimammography using effective multi-dimensional smoothing. *IEEE Trans. Nuc. Sci.*, 45(3):1273–9, June 1998.

kao:98:ksr [76] C-M. Kao, M. N. Wernick, and C-T. Chen. Kalman sinogram restoration for fast and accurate PET image reconstruction. *IEEE Trans. Nuc. Sci.*, 45(6):3022–9, December 1998.

lariviere:00:nrs [77] P. J. La Riviere and X. Pan. Nonparametric regression sinogram smoothing using a roughness-penalized Poisson

likelihood objective function. *IEEE Trans. Med. Imag.*, 19(8):773–86, August 2000.

kachelriess:01:gmd [78] M. Kachelrieß, O. Watzke, and W. A. Kalender. Generalized multi-dimensional adaptive filtering for conventional and spiral single-slice, multi-slice, and cone-beam CT. *Med. Phys.*, 28(4):475–90, April 2001.

villain:03:tde [79] N. Villain, Y. Goussard, J. Idier, and M. Allain. Three-dimensional edge-preserving image enhancement for computed tomography. *IEEE Trans. Med. Imag.*, 22(10):1275–87, October 2003.

august:04:srt [80] J. August and T. Kanade. Scalable regularized tomography without repeated projections. In *Proc. Intl. Parallel and Distributed Processing Symposium (IPDPS)*, volume 18, pages 3189–96, 2004.

pawitan:05:ngs [81] Y. Pawitan, V. Bettinardi, and M. Teras. Non-gaussian smoothing of low-count transmission scans for PET whole-body studies. *IEEE Trans. Med. Imag.*, 24(1):122–9, January 2005.

lariviere:05:ron [82] P. J. La Riviere and D. M. Billmire. Reduction of noise-induced streak artifacts in X-ray computed tomography through spline-based penalized-likelihood sinogram smoothing. *IEEE Trans. Med. Imag.*, 24(1):105–11, January 2005.

lariviere:06:pls [83] P. J. La Riviere, J. Bian, and P. A. Vargas. Penalized-likelihood sinogram restoration for computed tomography. *IEEE Trans. Med. Imag.*, 25(8):1022–36, August 2006.

thibault:06:arf [84] J-B. Thibault, C. A. Bouman, K. D. Sauer, and J. Hsieh. A recursive filter for noise reduction in statistical iterative tomographic imaging. In *Proc. SPIE 6065, Computational Imaging IV*, page 60650X, 2006.

soumekh:86:irt [85] M. Soumekh. Image reconstruction techniques in tomographic imaging systems. *IEEE Trans. Acoust. Sp. Sig. Proc.*, 34(4):952–62, August 1986.

karp:88:cfs [86] J. S. Karp, G. Muehllehner, and R. M. Lewitt. Constrained Fourier space method for compensation of missing data im emission computed tomography. *IEEE Trans. Med. Imag.*, 7(1):21–5, March 1988.

riviere:99:fvt [87] P. J. L. Riviere and X. Pan. Few-view tomography using roughness-penalized nonparametric regression and periodic spline interpolation. *IEEE Trans. Nuc. Sci.*, 46(4-2):1121–8, August 1999.

zamyatin:07:eot [88] A. A. Zamyatin and S. Nakanishi. Extension of the reconstruction field of view and truncation correction using sinogram decomposition. *Med. Phys.*, 34(5):1593–604, May 2007.

huesman:89:cfc [89] R. H. Huesman, E. M. Salmeron, and J. R. Baker. Compensation for crystal penetration in high resolution positron tomography. *IEEE Trans. Nuc. Sci.*, 36(1):1100–7, February 1989.

lewitt:89:fmf [90] R. M. Lewitt, P. R. Edholm, and W. Xia. Fourier method for correction of depth-dependent collimator blurring. In *Proc. SPIE 1092, Med. Im. III: Im. Proc.*, pages 232–43, 1989.

karuta:92:eod [91] B. Karuta and R. Lecomte. Effect of detector weighting functions on the point spread function of high-resolution PET tomographs. *IEEE Trans. Med. Imag.*, 11(3):379–85, September 1992.

wernick:92:stb [92] M. N. Wernick and C. T. Chen. Superresolved tomography by convex projections and detector motion. *J. Opt. Soc. Am. A*, 9(9):1547–53, September 1992.

liang:94:drr [93] Z. Liang. Detector response restoration in image reconstruction of high resolution positron emission tomography. *IEEE Trans. Med. Imag.*, 13(2):314–21, June 1994.

xu:98:aim [94] B. Xu, X. Pan, and C-T. Chen. An innovative method to compensate for distance-dependent blurring in 2D SPECT. *IEEE Trans. Nuc. Sci.*, 45(4):2245–51, August 1998.

kao:00:air [95] C-M. Kao, X. Pan, and C-T. Chen. Accurate image reconstruction using DOI information and its implications for the development of compact PET systems. *IEEE Trans. Nuc. Sci.*, 47(4-2):1551–60, August 2000.

alessio:06:aro [96] A. Alessio, K. Sauer, and P. Kinahan. Analytical reconstruction of deconvolved Fourier rebinned PET sinograms. *Phys. Med. Biol.*, 51(1):77–94, January 2006.

glick:94:ncf [97] S. J. Glick, B. C. Penney, M. A. King, and C. L. Byrne. Noniterative compensation for the distance-dependent detector response and photon attenuation in SPECT. *IEEE Trans. Med. Imag.*, 13(2):363–74, June 1994.

xia:95:fcf [98] W. Xia, R. M. Lewitt, and P. R. Edholm. Fourier correction for spatially variant collimator blurring in SPECT. *IEEE Trans. Med. Imag.*, 14(1):100–15, March 1995.

pan:96:aco [99] X. Pan, C. E. Metz, and C-T. Chen. A class of analytical methods that compensate for attenuation and spatially-variant resolution in 2D SPECT. *IEEE Trans. Nuc. Sci.*, 43(4-1):2244–54, August 1996.

kao:00:nim [100] C-M. Kao and X. Pan. Non-iterative methods incorporating a priori source distribution and data information for suppression of image noise and artefacts in 3D SPECT. *Phys. Med. Biol.*, 45(10):2801–19, October 2000.

tsui:79:asf [101] E. T. Tsui and T. F. Budinger. A stochastic filter for transverse section reconstruction. *IEEE Trans. Nuc. Sci.*, 26(2):2687–90, April 1979.

nowak:99:wdf [102] R. D. Nowak and R. G. Baraniuk. Wavelet-domain filtering for photon imaging systems. *IEEE Trans. Im. Proc.*, 8(5):666–78, May 1999.

edholm:88:irf [103] P. Edholm, G. T. Herman, and D. A. Roberts. Image reconstruction from linograms: implementation and evaluation. *IEEE Trans. Med. Imag.*, 7(3):239–46, September 1988.

magnusson:93:lao [104] M. Magnusson. *Linogram and other direct Fourier methods for tomographic reconstruction*. PhD thesis, Linkoping, Sweden, 1993.

axel:90:lrf [105] L. Axel, G. T. Herman, D. A. Roberts, and L. Dougherty. Linogram reconstruction for magnetic resonance imaging (MRI). *IEEE Trans. Med. Imag.*, 9(4):447–9, December 1990.

averbuch:08:aff-1 [106] A. Averbuch, R. R. Coifman, D. L. Donoho, M. Israeli, and Y. Shkolnisky. A framework for discrete integral transformations I—The pseudopolar Fourier transform. *SIAM J. Sci. Comp.*, 30(2):764–84, 2008.

averbuch:08:aff-2 [107] A. Averbuch, R. R. Coifman, D. L. Donoho, M. Israeli, Y. Shkolnisky, and I. Sedelnikov. A framework for discrete integral transformations II—The 2D discrete Radon transform. *SIAM J. Sci. Comp.*, 30(2):785–803, 2008.

kinahan:99:f3i [108] P. Kinahan, R. Clackdoyle, and D. Townsend. Fully-3D image reconstruction using planograms. In *Proc. Intl. Mtg. on Fully 3D Image Recon. in Rad. and Nuc. Med*, pages 329–32, 1999.

brasse:04:ff3 [109] D. Brasse, P. E. Kinahan, R. Clackdoyle, M. Defrise, C. Comtat, and D. W. Townsend. Fast fully 3-D image reconstruction in PET using planograms. *IEEE Trans. Med. Imag.*, 23(4):413–25, April 2004.

kazantsev:04:sag [110] I. G. Kazantsev, S. Matej, and R. M. Lewitt. System and gram matrices of 3-D planogram data. *IEEE Trans. Nuc. Sci.*, 51(5):2579–87, October 2004.

kazantsev:06:io2 [111] I. G. Kazantsev, S. Matej, and R. M. Lewitt. Inversion of 2D planogram data for finite-length detectors. *IEEE Trans. Nuc. Sci.*, 53(1):160–6, February 2006.

gullberg:86:raf [112] G. T. Gullberg, C. R. Crawford, and B. M. W. Tsui. Reconstruction algorithm for fan beam with a displaced center-of-rotation. *IEEE Trans. Med. Imag.*, 5(1):23–9, March 1986.

besson:96:cfb [113] G. Besson. CT fan-beam parametrizations leading to shift-invariant filtering. *Inverse Prob.*, 12(6):815–33, December 1996.

you:07:htb [114] J. You and G. L. Zeng. Hilbert transform based FBP algorithm for fan-beam CT full and partial scans. *IEEE Trans. Med. Imag.*, 26(2):190–9, February 2007.

herman:77:fir [115] G. T. Herman and A. Naparstek. Fast image reconstruction based on a Radon inversion formula appropriate for rapidly collected data. *SIAM J. Appl. Math.*, 33(3):511–33, November 1977.

lakshminarayanan:75:rfd [116] A. V. Lakshminarayanan. Reconstruction from divergent ray data. Technical Report 92, Dept. of Comp. Sci., State University of New York, Buffalo, NY, 1975.

chen:03:anf [117] G-H. Chen. A new framework of image reconstruction from fan beam projections. *Med. Phys.*, 30(6):1151–61, June 2003.

parker:82:oss [118] D. L. Parker. Optimal short scan convolution reconstruction for fan beam CT. *Med. Phys.*, 9(2):254–7, March 1982.

noo:02:irf [119] F. Noo, M. Defrise, R. Clackdoyle, and H. Kudo. Image reconstruction from fan-beam projections on less than a short scan. *Phys. Med. Biol.*, 47(14):2525–46, July 2002.

pan:99:onc [120] X. Pan. Optimal noise control in and fast reconstruction of fan-beam computed tomography image. *Med. Phys.*, 26(5):689–97, May 1999.

gullberg:79:tro [121] G. T. Gullberg. The reconstruction of fan-beam data by filtering the back-projection. *Comp. Graphics and Im. Proc.*, 10(1):30–47, May 1979.

feldkamp:84:pcb [122] L. A. Feldkamp, L. C. Davis, and J. W. Kress. Practical cone beam algorithm. *J. Opt. Soc. Am. A*, 1(6):612–9, June 1984.

katsevich:02:tef [123] A. Katsevich. Theoretically exact filtered backprojection-type inversion algorithm for spiral CT. *SIAM J. Appl. Math.*, 62(6):2012–26, 2002.

pan:04:aua [124] X. Pan, D. Xia, Y. Zou, and L. Yu. A unified analysis of FBP-based algorithms in helical cone-beam and circular cone- and fan-beam scans. *Phys. Med. Biol.*, 49(18):4349–70, September 2004.

chen:05:ane [125] G-H. Chen, S. Leng, and C. A. Mistretta. A novel extension of the parallel-beam projection-slice theorem to divergent fan-beam and cone-beam projections. *Med. Phys.*, 32(3):654–65, March 2005.

stierstorfer:04:wfa [126] K. Stierstorfer, A. Rauscher, J. Boese, H. Bruder, S. Schaller, and T. Flohr. Weighted FBP-A simple approximate 3D FBP algorithm for multislice spiral CT with good dose usage for arbitrary pitch. *Phys. Med. Biol.*, 49(11):2209–18, June 2004.

noo:04:ats [127] F. Noo, R. Clackdoyle, and J. D. Pack. A two-step Hilbert transform method for 2D image reconstruction. *Phys. Med. Biol.*, 49(17):3903–24, September 2004.

defrise:06:tht [128] M. Defrise, Frédéric Noo, R. Clackdoyle, and H. Kudo. Truncated Hilbert transform and image reconstruction from limited tomographic data. *Inverse Prob.*, 22(3):1037–54, June 2006.

xia:06:rfp [129] D. Xia, Y. Zou, and X. Pan. Reconstructions from parallel- and fan-beam data with truncations. In *Proc. SPIE 6142, Medical Imaging 2006: Phys. Med. Im.*, page 614222, 2006.

natterer:01:iot [130] F. Natterer. Inversion of the attenuated Radon transform. *Inverse Prob.*, 17(1):113–9, February 2001.

novikov:02:otr [131] R. G. Novikov. On the range characterization for the two-dimensional attenuated x-ray transformation. *Inverse Prob.*, 18(3):677–700, June 2002.

kunyansky:04:iot [132] L. A. Kunyansky. Inversion of the 3D exponential parallel-beam transform and the Radon transform with angle-dependent attenuation. *Inverse Prob.*, 20(5):1455–78, October 2004.

perry:01:chs [133] J. L. Perry and T. D. Gamble. Continuous high speed tomographic imaging system and method, 2001. US Patent 6,236,709.

lariviere:98:sbi [134] P. J. La Riviere and X. Pan. Spline-based inverse Radon transform in two and three dimensions. *IEEE Trans. Nuc. Sci.*, 45(4):2224–31, August 1998.

unser:99:sap [135] M. Unser. Splines: A perfect fit for signal and image processing. *IEEE Sig. Proc. Mag.*, 16(6):22–38, November 1999.

rattey:81:st2 [136] P. A. Rattey and A. G. Lindgren. Sampling the 2-D Radon transform. *IEEE Trans. Acoust. Sp. Sig. Proc.*, 29(4):994–1002, October 1981.

edholm:86:npo [137] P. R. Edholm, R. M. Lewitt, and B. Lindholm. Novel properties of the Fourier decomposition of the sinogram. In *Proc. SPIE 671, Physics and Engineering of Computerized Multidimensional Im. and Processing*, pages 8–18, 1986.

smith:85:mfo [138] K. T. Smith and F. Keinert. Mathematical foundations of computed tomography. *Appl. Optics*, 24(23):3950–7, 1985.

spyra:90:cti [139] W. J. T. Spyra, A. Faridani, K. T. Smith, and E. L. Ritman. Computed tomographic imaging of the coronary arterial tree-use of local tomography. *IEEE Trans. Med. Imag.*, 9(1):1–4, March 1990.

faridani:92:lt [140] A. Faridani, E. L. Ritman, and K. T. Smith. Local tomography. *SIAM J. Appl. Math.*, 52(2):459–484, April 1992.

faridani:97:lti [141] A. Faridani, D. V. Finch, E. L. Ritman, and K. T. Smith. Local tomography II. *SIAM J. Appl. Math.*, 57(4):1095–127, August 1997.

defrise:09:dot [142] F. C. Sureau and M. Defrise. Discretization of the two-step Hilbert transform for truncated data reconstruction. In *Proc. Intl. Mtg. on Fully 3D Image Recon. in Rad. and Nuc. Med*, pages 182–5, 2009.

mikhlin:57 [143] S. G. Mikhlin. *Integral equations and their applications to certain problems in mechanics, mathematical physics and technology*. Pergamon, New York, 1957.